Moroccan Journal of Chemistry
ISSN : 2351-812X
Copyright © 2023,
University of Mohammed Premier Oujda Morocco

Mor. J. Chem., 2023, Volume 11, Issue 01, Page 155-187
https://revues.imist.ma/index.php/morjchem

Synthesis, Characterization and Corrosion Inhibition Potential of Olefin Derivatives for Carbon Steel in 1M HCl: Electrochemical and DFT Investigations

Youssefi Y.[1], Oucheikh L.[1], Ou-ani O.[1], Jabha M.[2], Oubair A.[1] ,
Znini M.[1*] , Ebenso E.E.[3], Hammouti B.[4,5]

[1] *Moulay Ismail University of Meknes, Laboratory of Natural Substances & Synthesis and Molecular Dynamic, Faculty of Sciences and Techniques, Errachidia, Morocco,*
[2] *Moulay Ismail University of Meknes, Laboratory of chemical-physical, environmental and materials sciences, Faculty of Sciences and Techniques, Errachidia, Morocco,*
[3] *Centre for Materials Science, University of South Africa, Johannesburg 1710, South Africa.*
[4] *CREHEIO (Centre de Recherche de l'Ecole des Hautes Etudes d'Ingénierie Oujda/60000, Morocco).*
[5] *University Mohammed First, Faculty of Sciences, Laboratory of Applied Chemistry & Environment (LCAE) Department of Chemistry, BP 717, 60000 Oujda, Morocco*
** Corresponding author. E-mail address: m.znini@yahoo.fr or m.znini@umi.ac.ma*

Received *20 Dec 2022,*
Revised *10 Jan 2023,*
Accepted *11 Jan 2023*

Citation*: Youssefi Y., Oucheikh L., Ou-ani O., Jabha M., Oubair A., Znini M., Hammouti B. (2023) Synthesis, Characterization and Corrosion Inhibition Potential of Olefin Derivatives for Carbon Steel in 1M HCl: Electrochemical and DFT Investigations, Mor. J. Chem., 14(1), 155-187. Doi: https://doi.org/10.48317/IMIST.PRSM/morjchem-v11i1.37306*

Abstract: This research aims to evaluate the anticorrosive properties of three olefins derivatives synthesized by the microwave oven technique in a dry environment. These olefins have been identified using different analytical methods, including NMR, IR and XRD. The corrosion inhibition of these compounds for carbon steel in 1 M HCl solution was studied using potentiodynamic polarization (PDP) curves, electrochemical impedance spectroscopy (EIS), scanning electron microscopy (SEM) coupled with energy dispersive X-ray spectroscopy (EDX). The experimental results show that the tested compounds are good corrosion inhibitors for steel in an acidic media. Furthermore, the inhibition efficiency increased with increasing inhibitor concentration and decreased with increasing temperature. The PDP study showed the mixed type nature of these inhibitors, whereas thermodynamic parameters suggested that their adsorption obeys the Langmuir isotherm model. The EIS measurements revealed that the corrosion of the steel is produced by a single mechanism, which is charge transfer. SEM with EDX analysis confirmed the protection of the steel surface by the adsorption of the inhibitors. The relationship between the electronic properties of the inhibitors and the protective ability was further discussed using DFT calculations. Both experimental and theoretical results are well compatible and complement each other well.

Keywords: α-arylidene-γ-butyrolactones; Microwave; Mineral support; Corrosion inhibition; DFT.

1 Introduction

Steel is one of the materials that is utilized the most, especially in the automotive, industrial, steel construction, tanks and transport of petroleum products (Solmaz 2014; Bouanis et al. 2016; Titi et al. 2018). Despite its wide field of application, the dissolution and the destruction of this metal can occur in aggressive environments, especially in acid solutions. Several means have been developed to protect

metal against corrosion, use of corrosion inhibitors in corrosive conditions is one of the most beneficial (Ait Chikh *et al.* 2005; Chebabe *et al.* 2004; Bouklah *et al.* 2006; Lgaz *et al.* 2020). The easiest and most efficient technique of prevention to control and slow down corrosion in aggressive environments without compromising the properties of the metal is the use of organic molecules, especially heterocyclic ones, as corrosion inhibitors (Fateh *et al.* 2020). These compounds contain heteroatoms (N, O, S and P) and aromatic systems that encourage the inhibitor's adsorption onto the surface of the metal, creating a barrier between the solution and the metal (Wang *et al.* 2021).

The literature mentions different techniques for the synthesis of heterocycle compounds, such as the classical technique (reflux heating) (Častulík *et al.* 2001), the microwave oven technique (Tambe *et al.* 2021) and ultrasound (Thari *et al.* 2020). Among these heterocycles are the lactone derivatives, The importance of these compounds as building blocks in the synthesis of bioactive compounds has drawn researchers' attention (Mehl *et al.* 2010). Thus, they are known in therapy for their rich pharmacological potential: antibiotics (Reutrakul *et al*. 2004), analgesics (de Souza *et al.* 2005) and anti-tumor (Romagnoli *et al.* 2007).

In this study, we were interested in the synthesis and characterization of a series of dipolarophiles namely: α-benzelidenyl-γ-butyrolactone (**3a**), α-(p-methylbenzelidenyl)-γ-butyrolactone (**3b**), α-(p-methoxybenzelidenyl)- γ-butyrolactone (**3c**) by condensation of γ-butyrolactone with arylaldehydes, using a microwave oven technique. Additionally, the corrosion inhibiting properties of these obtained products on carbon steel were tested in a 1 M HCl solution using electrochemical methods such as potentiodynamic polarisation (PDP) curves and electrochemical impedance spectroscopy (EIS) measurements. Scanning electron spectroscopy (SEM) was performed to analyze the corroded surfaced. Moreover, the adsorption of the tested compounds follows the Langmuir isotherm. Quantum chemical calculations using the density functional theory (DFT) method were conducted to explain the correlation between the electronic properties of inhibitors and their corrosion-inhibiting power.

2 Materials and Methods

2.1 Synthesis of olefins

2.1.1 General procedure

In a 250 mL Erlenmeyer flask, 3 g (34.9 mmol) of γ-butyrolactone (**1**), 3.7 g (34.9 mmol) of arylaldehydes (**2**), and 0.84 g (34.9 mmol) of sodium hydride dissolved in 5 mL of ethanol and 5 g of natural clay from the Daraa-Tafilalet region were mixed. The mixture was activated for 5 minutes using 600 W by microwave power. The organic matter is recovered by diethyl ether, the clay is removed by filtration and the solvent was evaporated by rotavapor. The obtained products were purified by recrystallization in absolute ethanol (**Erreur ! Source du renvoi introuvable.**).

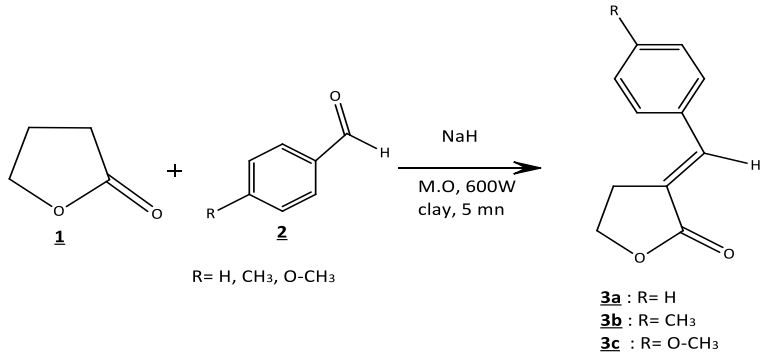

Figure 1. Synthesis of olefins derivatives **3a**, **3b** and **3c.**

2.1.1.1 α-benzelidenyl- γ-butyrolactone (3a)

White product, Mp = 114 °C, yield = 90%. **^{1}H NMR (300 MHz, DMSO)**, δ (in ppm): 2.52 (m, 2H, $^{4}CH_2$); 4.443 (m, 2H, $^{5}CH_2$); 7.31 - 7.58 (m, 6H, $CH_{unsaturated}$). **^{13}C NMR (75 MHz, DMSO),** δ (in ppm): 26.90 (C^4); 65.49 (^5C); 125.08 - 128.92 - 129.12 - 129.69 - 129.96 - 134.45 - 134.63 ($C_{unsaturated}$); 171.93 (C=O). **IR (KBr)**, (υ in cm^{-1}): υ (C=C) = 1649.82; υ (C=O) =1737.07; υ (CH sp^3) = 2928.57; υ (CH sp^2) = (3048.42-3088.39).

2.1.1.2 *α- (p-methylbenzelidényl)-γ-butyrolactone (3b)*

White product, Mp = 115 °C, yield = 92%. **^{1}H NMR (300 MHz, DMSO),** δ (in ppm): 2.36 (s, 3H, CH_3), 3.23 (m, 2H, $^{4}CH_2$); 4.442 (m, 2H, $^{5}CH_2$); 7.30 - 7.55 (m, 6H, $CH_{unsaturated}$). **^{13}C NMR (75 MHz, DMSO),** δ (in ppm): 20.98 (CH_3); 26.90 (C^4); 65.40 (C^5); 123.83 - 129.53 - 129.99 - 131.74 - 134.67 - 139.68 ($C_{unsaturated}$); 172.03 (C=O). **IR (KBr),** (υ in cm^{-1}): υ (C=C) = 1651.71; υ (C=O) = 1732.22; υ (CH sp^3) = 2990.07; υ (CH sp^2) = (3018.63-3097.63).

2.1.1.3 α-(p-methoxybenzelidényl)-γ-butyrolactone (3c)

White product, Mp = 124 °C, yield = 90%. **^{1}H NMR (300 MHz, DMSO),** δ (in ppm): 3.20 (m, 2H, $^{4}CH_2$); 3.31 (s, 3H, OCH_3); 4,441 (m, 2H, $^{5}CH_2$); 7.04 - 7.61 (m, 6H, $CH_{unsaturated}$). **^{13}C NMR (75 MHz, DMSO**), δ (in ppm): 26.80 (C^4); 55.28 (OCH_3); 65.29 (C^5); 114.40 - 114.82 - 121.90 - 127.10 - 131.81 - 134.54 - 160.37 ($C_{unsaturated}$); 172.18 (C=O). **IR (KBr), (**υ in cm^{-1}): υ (C=C) = 1653.02; υ (C=O) = 1732.21; υ (CH sp^3) = 2990.07-3000.76; υ (CH sp^2) = 3065.31.

2.2. Corrosion inhibition study

2.2.1 Material and corrosive solution

In this work the steel used is composed of percentage atomic weights as following: %C: 0.2; %N: 0.07; %S: 0.05; %P: 0.005; and rest Fe. Before corrosion studies, the steel coupons of an area of 1 cm^2 were rubbed with emery papers of different grades (from 300 to 2400) and washed with distilled water. The 1M HCl corrosive medium was prepared by diluting commercial acid with distilled water. The organic compounds tested as the corrosion inhibitors are the synthesized olefins **3a**, **3b** and **3c**. Each corrosion inhibitor was tested at different concentrations (5×10^{-5}, 10^{-4}, 5×10^{-4}, 10^{-3}M).

2.2.2 Electrochemical measurements

PDP curves and EIS measurements were made using a Biologic SP-150 potentiostat, controlled by EC-Lab software. These measurements were made with a conventional three electrode system, the carbon steel sample as the working electrode, the reference electrode in Ag/AgCl, and the counter electrode in platinum. Prior to the electrochemical test, the steady state open circuit potential (OCP) was generated by immersing the working electrode in 1 M HCl medium for 1800 s. The PDP curves were performed from -1 V to 0 V at a scan rate of 10^{-3} V/s and the following relationship (1) was used to compute the corrosion inhibition efficiency (IE) (%).

$$EI(\%)=\frac{i_{corr}^{0}-i_{corr}}{i_{corr}^{0}}\times 100 \qquad (1)$$

i_{corr} and i_{corr}^{0} are the corrosion current density in the presence and absence of inhibitor, respectively.

However, the EIS measurements were made with an amplitude of 10 mV over a frequency range of 100 kHz to 10 mHz. An equivalent circuit was used to correct and analyze the impedance data. The IE (%) is additionally calculated using relationship (2), from the charge transfer resistance (Mobin et al. 2022):

$$EI_{imp}\%=\frac{R_{ct}-R_{ct}^{0}}{R_{ct}}\times 100 \qquad (2)$$

Where, R_{ct} and R_{ct}^{0} are the charge transfer resistance values in the presence and absence of inhibitor, respectively.

2.2.3 Surface analysis

The composition and surface morphology of the carbon steel samples were studied by SEM spectroscopy coupled with EDX spectroscopy. The surface analysis was performed for the identical steel plates with a surface of 1 cm^2 rubbed by emery paper, after immersion in 1M HCl solution with and without best concentration (10^{-3}M) of each inhibitor (**3a**, **3b** and **3c**) for 20 h, using the JSMIT500HR electron microscope with an acceleration energy of 0.5 to 30 KV.

2.2.4 DFT calculations

The DFT calculations utilizing the B3LYP/6-31G (d, p) basis were used to optimize the geometry and calculate the total energy of the tested compounds **3a**, **3b** and **3c**. The DFT method has shown to be useful in revealing information on chemical reactivity in terms of general molecular properties (Umar 2022), such as HOMO, LUMO, energy gap (ΔEg), electronegativity (χ), chemical potential (μ), The hardness (η), The overall softness (S), The global electrophilicity index (ω), The electronic charge transfer (ΔN) and the associated energy change (ΔE), which are calculated via the following relationships (Olasunkanmi et al. 2016):

$$\Delta Eg = E_{LUMO} + E_{HOMO} \qquad (3)$$

$$\chi = -\mu = -\frac{E_{LUMO} + E_{HOMO}}{2} \qquad (4)$$

$$\eta = \frac{E_{LUMO} - E_{HOMO}}{2} \qquad (5)$$

$$S = \frac{1}{\eta} \qquad (6)$$

$$\omega = \frac{\mu^2}{2\eta} \qquad (7)$$

$$\Delta N = \frac{\chi_{metal} - \chi_{mol}}{2(\eta_{metal} + \eta_{mol})} = \frac{\Phi - \chi_{mol}}{2\eta_{mol}} \qquad (8)$$

$$\Delta E = -\frac{(\chi_{metal} - \chi_{mol})^2}{4(\eta_{metal} + \eta_{mol})} = \frac{(\Phi - \chi_{mol})^2}{4\eta_{mol}} \qquad (9)$$

The electronegativity of the metal surface is replaced by the work function of the iron surface Φ, which is theoretically equal to 4.82 eV and the hardness η of the metal, which is equal to 0 eV for bulk metals (Kovačević and Kokalj 2011).

3 Results and discussion

3.1 Characterization of synthesized olefins

The structures of the synthesized compounds were established according to ^{1}H, ^{13}C NMR and IR spectral data. Indeed, the analysis of the ^{1}H NMR spectra (**Fig. 2**) of the obtained compounds **3a-c** shows the signals of the unsaturated carbons which process respectively in the interval (7.43-8.33 ppm), (7.30-7.55 ppm) and (7.04-7.61 ppm) under different massive according to the nature of the substituent on the aromatic nucleus.

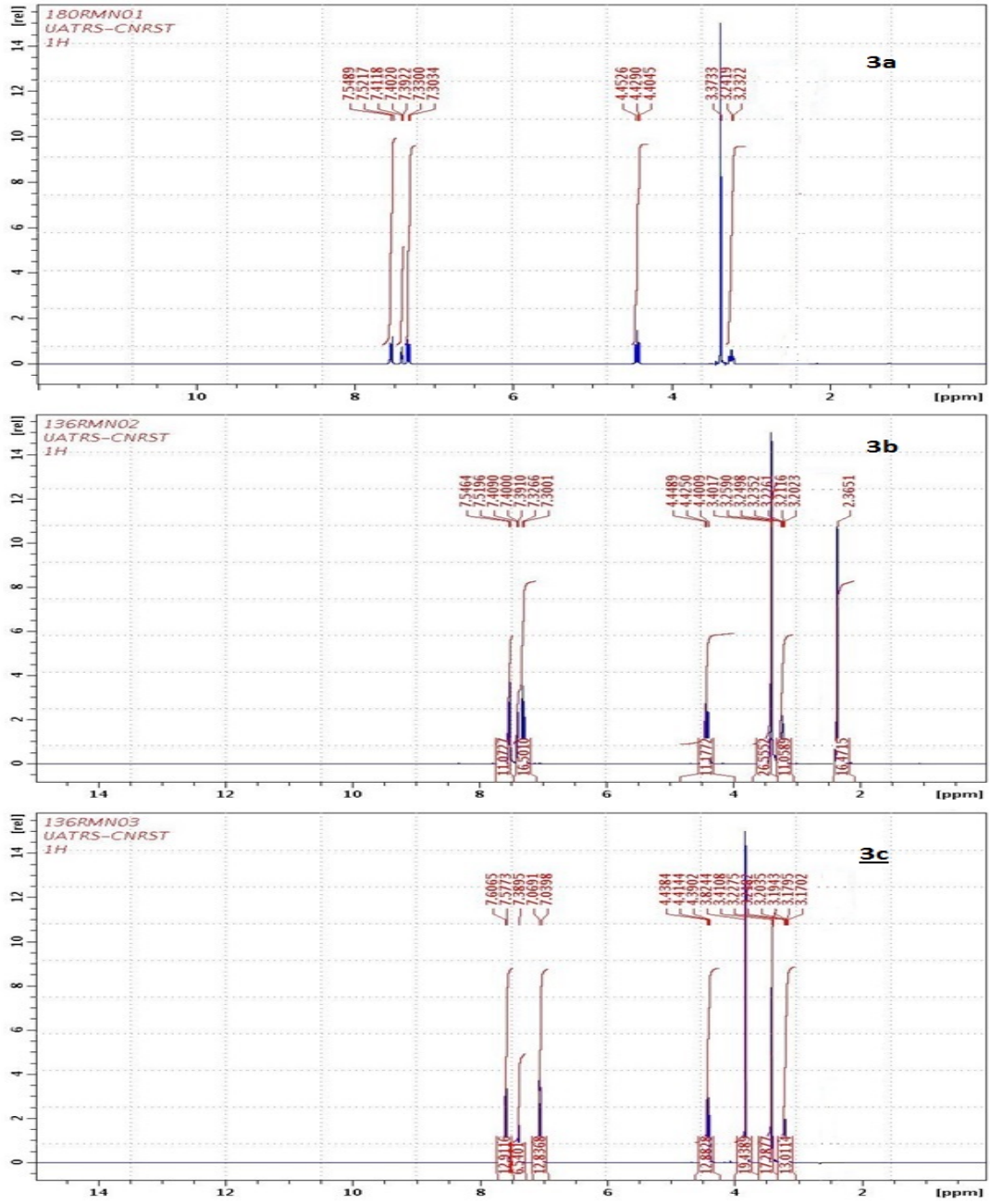

Figure 2. ^{1}H-NMR spectrum of olefins derivatives **3a**, **3b** and **3c**

The two protons of the two C^4 carbons appear as a multiple centered respectively at 2.52 ppm, 3.23 ppm and 3.20 ppm while the protons of C^5 are a little shielded compared to those of C^4 and they appear as a multiple at 4.443 ppm, 4.442 ppm and 4.441 ppm respectively. Methyl group protons of product **3b** are seen as a singlet at 2.36 ppm. The protons of the methoxy group of **3c** appear as a singlet at 3.31 ppm. Furthermore, the ^{13}C NMR spectra and the dept (**Figs S1-S6**) show that the structures of the 3a-c products are characterized by the presence of a carbonyl group (C=O) which resonates respectively at 171.93, 172.03 and 172.18 ppm in the area of the weak magnetic field. These spectra confirm that the three structures **3a-c** each contain two methines groups (-CH_2) which appear respectively at (26.90 and 65.49 ppm), (26.90 and 65.40) and (26.80 and 65.29 ppm) which confirms the disappearance of one of these from the starting precursor (γ-butyrolactone). For the two compounds **3b** and **3c**, we note the presence of a third hybridized carbon sp^3 at 20.98 ppm characterizing the methyl group of **3b** while for product **3c**, this carbon appears at 55.28 ppm justifying the presence of the methoxy group. The IR spectra of the **3a-c** products (**Figs S7-S9**) allow for the identification of many features, including a strong absorption band typical of a carbonyl group that occurs at positions 1737.07, 1732.27 and 1732.21 cm^{-1}, respectively. Moreover, the structure of compound **3b** as monocrystalline was confirmed by a crystallographic radio study (Erreur ! Source du renvoi introuvable.**3**). The crystal data are grouped in **Tables S1-S6**.

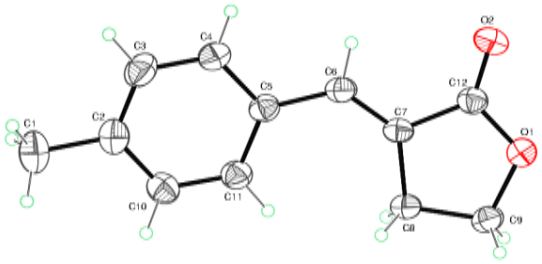

Figure 3. Crystallographic structure of compound **3b**

3.2 Electrochemical study

3.2.1 OCP study

Erreur ! Source du renvoi introuvable.4 depicts the change in OCP as the carbon steel is immersed in a 1 M HCl solution at 298 K with and without different concentrations of the inhibitors **3a**, **3b** and **3c**. As seen, the corrosion potential (Eocp) of the carbon steel immersed in the 1M HCl acid solution with and without inhibitor shows an increase to reach a quasi-stationary state at about 1800 s of immersion time, which indicates that the steel/solution interface has reached a stable condition. Furthermore, a shift of E_{corr} towards more positive values is noted with an increasing concentration of three inhibitors. These variations may be explained by the development of a layer on the electrode. (Huang et al. 2022). This may also indicate that our inhibitors can slow down the reactions that occur on the surface of electrode, such as the oxidation of iron and the reduction of H^+ from hydrochloric acid (de Souza and Spinelli 2009).

3.2.2 PDP study

Polarization curves of carbon steel in 1 M HCl medium without and with the addition of inhibitors **3a**, **3b** and **3c** at various concentrations at 298 K, are presented in Erreur ! Source du renvoi introuvable.**5**.

The analysis of **Erreur ! Source du renvoi introuvable.**5 demonstrates that the cathodic and anodic current densities are reduced when the inhibitors **3a**, **3b**, and **3c** are added to the corrosive medium.

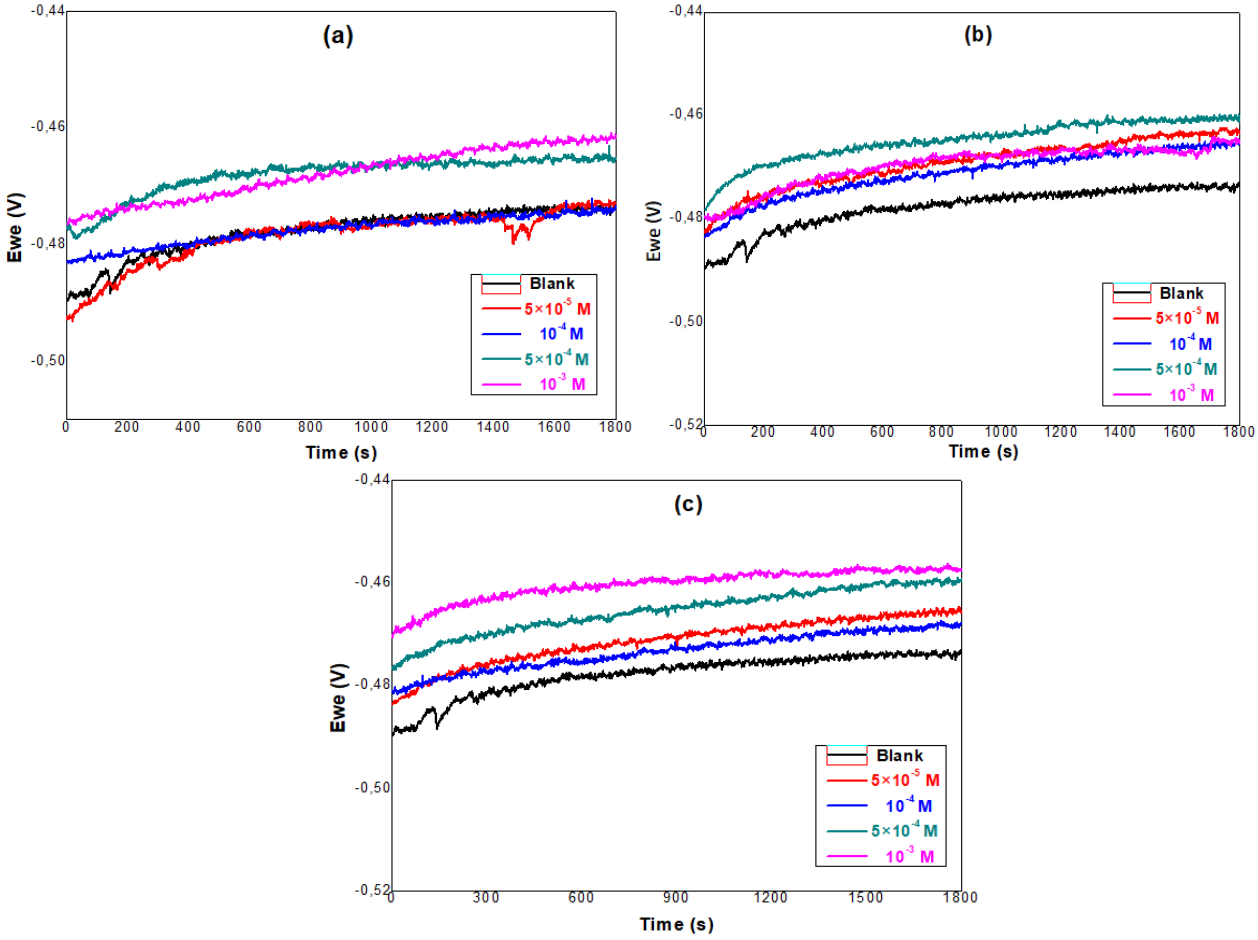

Figure 4. OCP–time curves for carbon mild steel in 1 M HCl with and without inhibitors **3a** (a), **3b** (b) and **3c** (c) at different concentrations.

These results also show that the E_{corr} values vary after the addition of the inhibitors and that the tested compounds can be categorized as inhibitors of mixed types having a cathodic action. The corresponding electrochemical characteristics, such as the cathodic and anodic Tafel slopes (βc, βa), corrosion potential (E_{corr}), corrosion current density (i_{corr}), Surface coverage (θ) and corrosion inhibition efficiency EI (%), are collected in **Table 1**. The equation (10) is used to compute the values of (θ):

$$\theta = \frac{i^0_{corr} - i_{corr}}{i^0_{corr}} \qquad (10)$$

The analysis of **Table 1** shows the decrease in corrosion current densities with the presence of each inhibitor. Consequently, the inhibition efficiency increase. Moreover, the higher the concentration, the more the values of the corrosion current density (i_{corr}) decrease, reaching lower values equal to 68.13, 82.27 and 95.18 mA/cm^2 for **3c**, **3b** and **3a** respectively, at a concentration of 10^{-3} M. This indicates that in an aggressive environment, as the inhibitor concentration increases, metal dissolution and hydrogen formation decrease due to protective film formed by tested inhibitors on the metal surface (Hafez and al. 2019). The E_{corr} for the three inhibitors are relatively shifted to negative and positive

values (cathodic and anodic directions) in the presence of the inhibitors compared to the uninhibited acid.

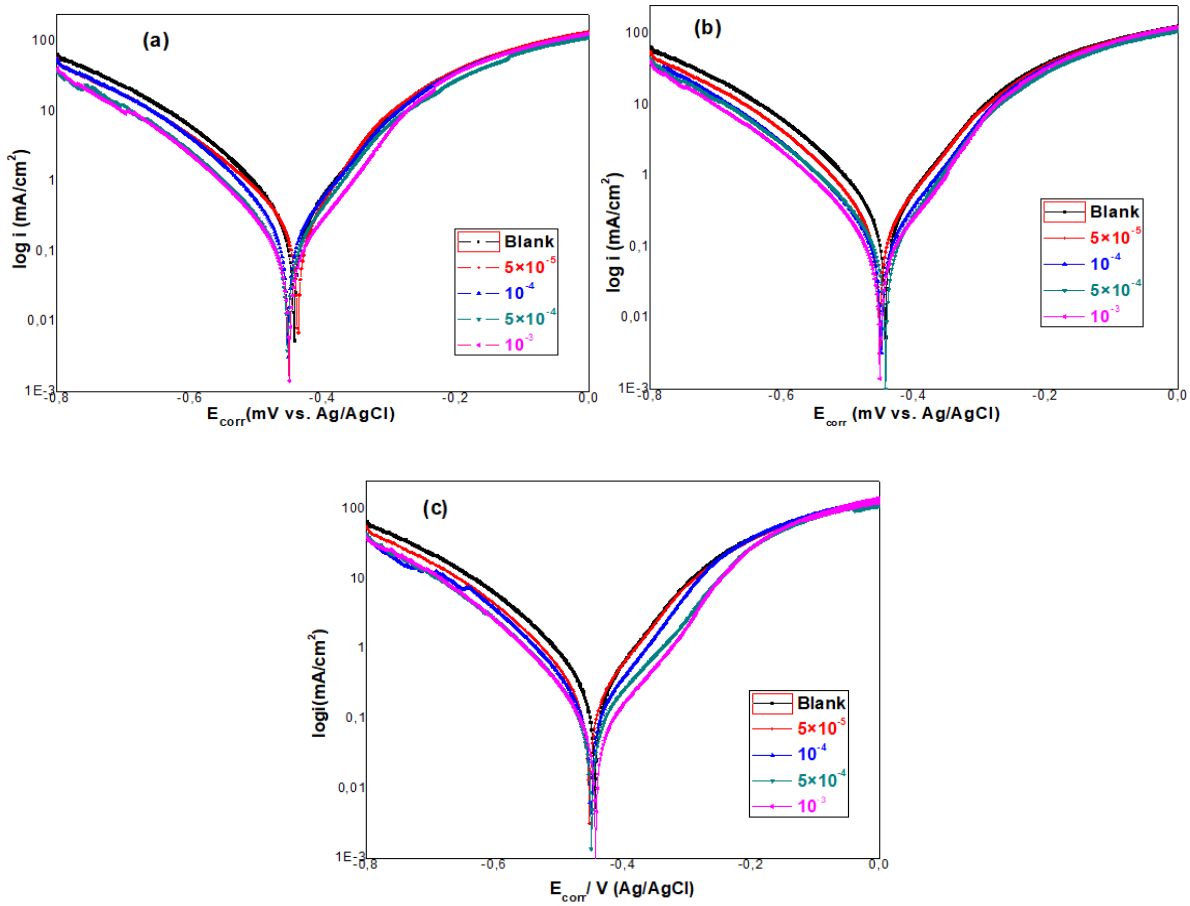

Figure 5. Polarization curves for carbon steel in 1 M HCl with and without inhibitors **3a** (a), **3b** (b) and **3c** (c) at different concentrations.

Table 1 PDP parameters for the corrosion of carbon steel in 1 M HCl with and without inhibitors **3a**, **3b** and **3c** at different concentrations.

Inhibitor	C (M)	E_{corr}(mV vs. Ag/AgCl)	i_{corr}(mA/cm^2)	βc(mV/dec)	βa(mV/dec)	θ	EI (%)
Blank	0	-443.37	351.38	130.9	108.6	-	-
(**3a**)	5×10^{-5}	-437.56	223.37	116.8	81.8	0.36	36.43
	10^{-4}	-452.39	197.22	103.3	95.7	0.44	43.87
	5×10^{-4}	-453.08	121.67	105.8	87.7	0.65	65.37
	10^{-3}	-451.01	95.18	104.8	88.1	0.73	72.91
(**3b**)	5×10^{-5}	-452.38	208.46	109.5	97.5	0.41	40.67
	10^{-4}	-449.67	130.43	109.5	90.7	0.63	62.88
	5×10^{-4}	-443.21	107.45	106.1	85.6	0.69	69.42
	10^{-3}	-451.46	82.27	104.3	85.2	0.76	76.59
(**3c**)	5×10^{-5}	-452.39	203.15	106.4	96.9	0.42	42.18
	10^{-4}	-449.70	131.99	105.7	92.4	0.62	62.43

	5×10^{-4}	-448,88	102,16	107	104,7	0,71	70,92
	10^{-3}	-442,34	68,13	97,6	93,1	0,81	80,61

According to the literature (Anusuya et al. 2017), inhibitors are classified into two types, cathodic and anodic, where the difference between E_{corr} (presence of the inhibitor) and E_{corr} (without inhibitor) is greater than 85 mV, On the other hand, if the difference is less than 85 mV, the inhibitor becomes of mixed type (Ansari et al. 2014). In our case, the three inhibitors (**3a**, **3b**, and **3c**) had a difference of less than 13 mV, indicating that they are mixed-type inhibitors with a predominant cathodic effect. In addition, from the data in **Table 1**, we find that the three inhibitors show remarkable inhibitory efficiencies at 72.91; 76.59 and 80.61%, respectively when tested at 10^{-3} M. The methoxy group (O—CH_3) in compound **3c**'s structure may be responsible for its high efficacy.

3.2.3 EIS measurements

The EIS method offers a lot of information about the mode of action of inhibitors on the metal surface (Abdul Rahiman and Sethumanickam 2017). According to this technique, all the Nyquist diagrams (Erreur ! Source du renvoi introuvable.**6 (a, b, c)**) show that in the absence of inhibitors, there was just one capacitive loop found, and it was caused by a charge transfer that took place on the steel surface. (Rbaa *et al.* 2019). In the presence of the studied inhibitors, the size of this loop increases with increasing concentration of each inhibitor. It is a result of an inhibitor layer developing on a metal surface. These results are confirmed by the bode diagrams (Erreur ! Source du renvoi introuvable.**6 (d, e, f)**). At low frequencies, the impedance increases with increasing concentration of the inhibitors **3c, 3b**, and **3a**. This means that at higher concentrations, the inhibitor molecules are adsorbed on the steel surface, forming a protective layer that inhibits the charge transfer. It is also noticed that for the three inhibitors, the phase angles increase with the increase of the inhibitor concentration. This demonstrates that the inhibitor molecules **3a**, **3b** and **3c** that are adsorbed on the metal surface provide protection (Loganathan *et al.* 2021).

The phase angle curves of the three inhibitors (**3a**, **3b,** and **3c)** show maximum phase angles of 63.83°, 61.87° and 64.41°, respectively at the concentration of 10^{-3} M. This shows that the inhibitory capacities of these three compounds approach the ideal capacity which maximum phase angle is around 90° (Ma *et al.* 2017). **Erreur ! Source du renvoi introuvable.7** shows that the deduced equivalent circuit is composed of a constant phase element (CPE) in parallel with a charge transfer resistance Rct, The assembly is in series with a small resistance corresponding to the resistance of the electrolyte (Rs) *(Ramezanzadeh et al.* 2014). The impedance function Z_{CPE} of the CPE is calculated as follows:

$$Z_{CPE} = \frac{1}{Y_0 \times (i\times \omega)^n} \qquad (11)$$

The following estimates may be made for the double layer capacity (C_{dl}) values (Ramezanzadeh *et al.* 2014):

$$C_{dl} = Y_0(\omega_{max})^{n-1} \qquad (12)$$

With, ω is the angular frequency (rad/s), ω_{max} the frequency at which the imaginary impedance quantity has reached the maximum value (rad s^{-1}), i the imaginary unit ($i^2 = -1$), Y_0 the magnitude of the CPE and n the phase shift related to the degree of surface inhomogeneity, with $-1 \leq n \leq +1$, the CPE is regarded as a pure capacitor, a real resistance, and an inductance for n = 1, 0, and -1, respectively

(Dagdag *et al.* 2019). The values of the various electrochemical parameters Rct, Rs, n and Cdl as well as the inhibitory efficiency IE (%) are resumed in **Table 2**. From **Table 2**, we noted that for each inhibitor, the value of Rct increases with increasing inhibitor concentration. The values of the capacities of the double layers (Cdl) decreased. This can be accounted for by the inhibitor molecules adhering to the substrate's surface and putting up a barrier to protect the metal from the corrosive solution.

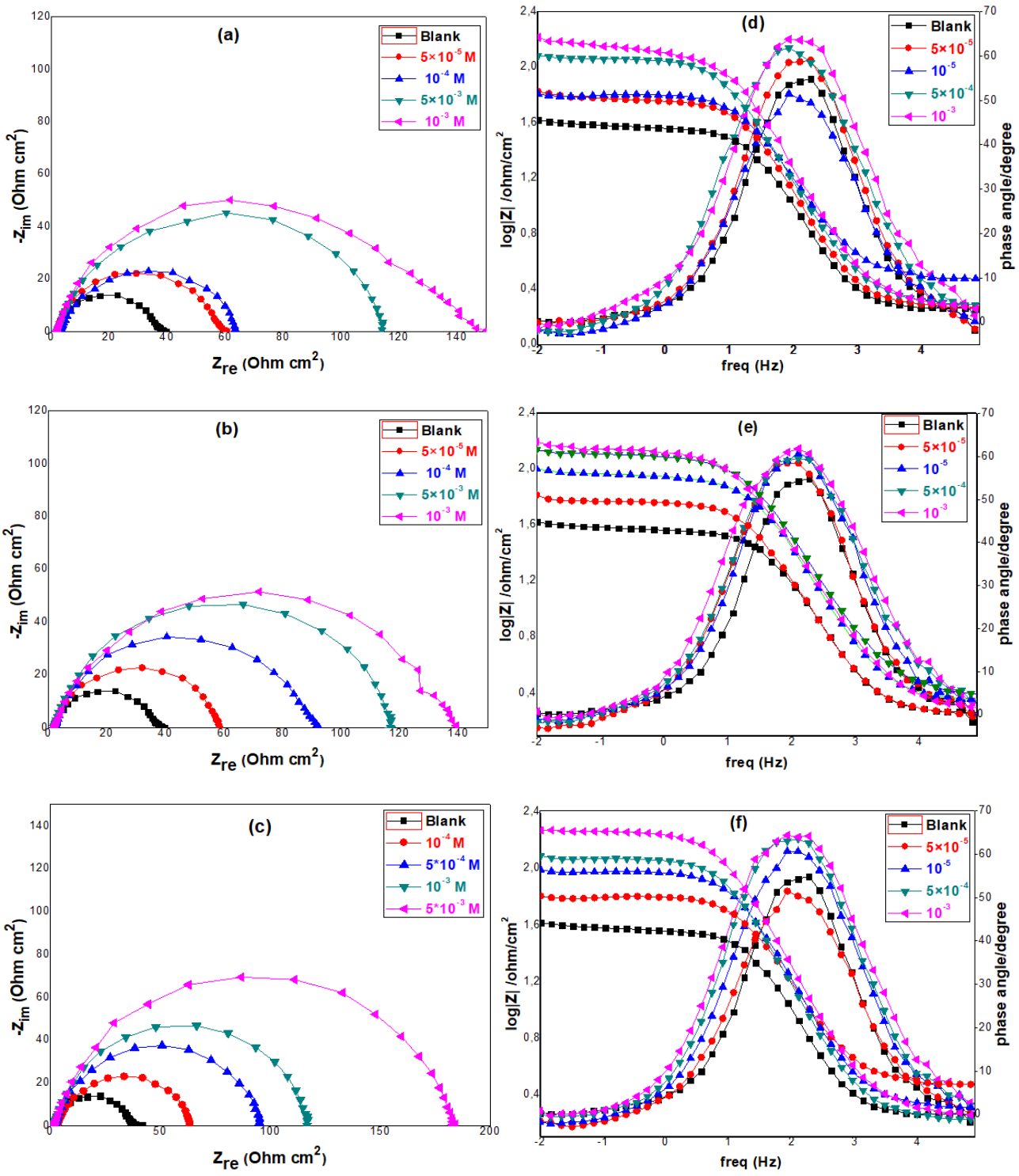

Figure 6. Nyquist plots (a, b,c) and Bode plots (d,e,f) for carbon steel in 1 M HCl solution in the absence and presence of different concentrations of inhibitors 3a (a,d), 3b (b,e) and 3c (c,f)

These results show that increasing the concentrations of inhibitors increases their inhibitory efficiency to reach maximum values of approximately 81, 75 and 74% at a concentration of 10^{-3}M for **3c**, **3b** and **3a**, respectively. This is accompanied by the increase in the number of molecules adsorbed on the metal surface which allows better coverage of the steel surface (Karthikaiselvi and Subhashini 2014).

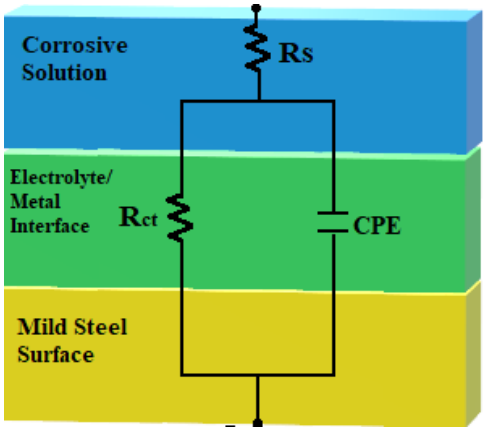

Figure 7. Equivalent circuit model used to fit EIS data

Table 2 EIS parameters for the corrosion of carbon steel in 1 M HCl with and without inhibitors **3a**, **3b** and **3c** at different concentrations.

Inhibitor	C (M)	R_s (Ω cm^2)	R_{ct} (Ω cm^2)	n	C_{dl} (µF cm^{-2})	IE %
Blank	0	1.80	34.59	0.867	200	-
(**3a**)	5×10^{-5}	1.87	56.78	0.865	166	39.08
	10^{-4}	2.98	62.09	0.806	150	44.29
	5×10^{-4}	1.95	115.1	0.828	167	69.95
	10^{-3}	1.92	136.5	0.807	145	74.66
(**3b**)	5×10^{-5}	1.79	57.29	0.856	182	39.62
	10^{-4}	2.23	87.92	0.851	128	60.66
	5×10^{-4}	1.71	116.9	0.853	154	70.41
	10^{-3}	1.88	138.1	0.828	130	74.95
(**3c**)	5×10^{-5}	3.82	57.53	0.807	148.2	39.87
	10^{-4}	3	89.36	0.843	138	61.29
	5×10^{-4}	2.75	112.4	0.853	125.9	69.22
	10^{-3}	3.85	175.7	0.835	124.3	80.31

3.3 Adsorption isotherm

It has been highlighted that the adsorption of organic substances on metal surfaces explains how they can prevent metal corrosion. The kind of adsorption isotherm can reveal details about the characteristics of the inhibitors that have been put to the test as well as the adsorption phenomena (Eid et al. 2020). Different types of isotherms (Temkin, El-Awady, Freundlich, Frumkin, and Langmuir) were tested (He *et al.* 2020). The Langmuir adsorption isotherm is the most appropriate based on the values of the regression coefficient (R^2). We used this model to explore the adsorption mechanism of

the inhibitors **3a**, **3b**, and **3c** on the metal surface. To fit the Langmuir model, we use the potentiodynamic polarization data. Its expression is as follows (Gao *et al.* 2020):

$$\frac{C}{\theta} = \frac{1}{K_{ads}} + C \qquad (13)$$

The plot of C/Θ as a function of inhibitor concentration is shown in Erreur ! Source du renvoi introuvable.**8** where the K_{ads} values were determined. $\Delta G°_{ads}$ is determined by the following relationship (14):

$$K_{ads} = \frac{1}{55.5}\exp\left(-\frac{\Delta G^0_{ads}}{RT}\right) \qquad (14)$$

With T: the absolute temperature and R: the perfect gas constant.

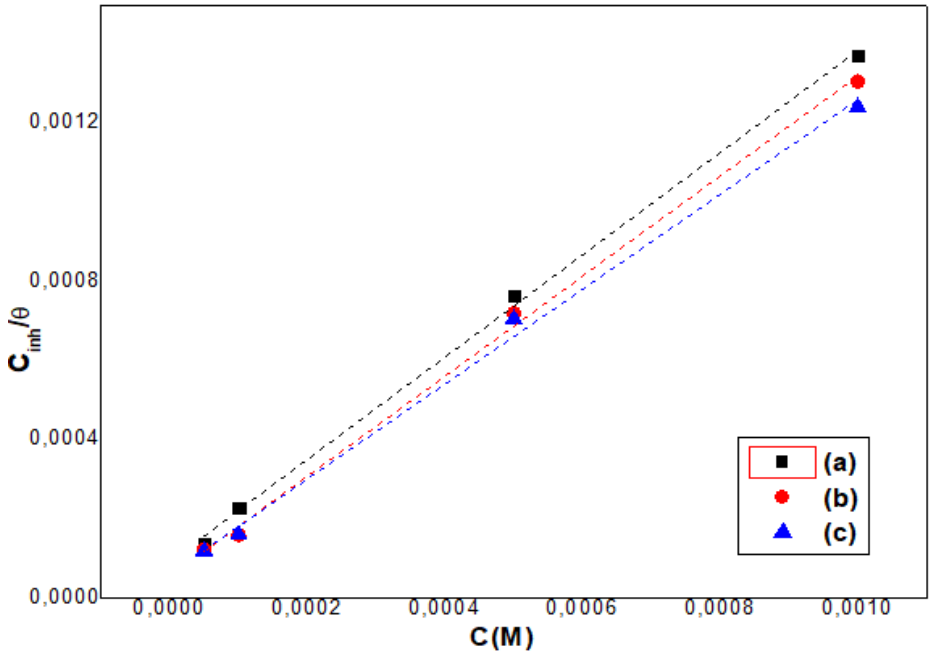

Figure 8. Langmuir adsorption curve of **3a** (a), **3b** (b) and **3c** (c)

The results of the calculated Langmuir adsorption isotherms are listed in **Table 3**. The linear regression coefficients R^2 of this model are 0.9967, 0.9991, and 0.9971 for inhibitors **3c**, **3b** and **3a** respectively. The large values of the constant K_{ads} for the three inhibitors indicate the strong adsorption capacity of the inhibitors on the carbon steel surface (Farahati *et al.* 2020).

Table 3 Thermodynamic parameters of adsorption of inhibitors **3a**, **3b** and **3c** on the carbon steel in 1M HCl.

Inhibitor	R^2	K_{ads} (L.mol^{-1})	$\Delta G°_{ads}$ (KJ.mol^{-1})
3a	0.998	10811.97	-34.33
3b	0.997	18079.25	-32.87
3c	0.995	16235.87	-33.95

The values of ΔG^0_{ads} are -33.95, -32.78, and -34.33kJ/mol for **3c**, **3b** and **3a** respectively. The negative values of ΔG^0_{ads} indicate the spontaneous adsorption of the molecules of the inhibitors **3a**, **3b** and **3c** on the metal surface with a strong interaction (Bayol *et al.* 2008). There are two types of inhibitor's adsorptions on the surface of metals: chemisorption, which is the formation of coordination or dative

bonds between the molecules of inhibitors and the metal, has binding energy less than or equal to -40 kJ/mol. And physisorption, which occurs through secondary bonds (Van Der Waals interaction) with an energy of the order of -20 kJ/mol (Farahati *et al.* 2020). In our study, the values of ΔG^0_{ads} for the three inhibitors are between -20 kJ/mol and -40 kJ/mol. Therefore, the adsorption of the inhibitors on the metal follows both chemical and physical adsorption (Fernine *et al.* 2022).

3.4 Effect of temperature

One of the kinetic elements investigated to show the kind of inhibitor adsorption on the steel surface is the impact of temperature on the corrosion behavior of carbon steel (chemisorption or physisorption) (Ouici *et al.* 2017). To study the effect of this factor on the inhibition efficiency, the potentiodynamic measurements were performed in a temperature range between 298 K and 328 K with and without 10^{-3}M of compound **3c** selected as the best inhibitor. The polarization curves at different temperatures are presented in Erreur ! Source du renvoi introuvable.**9**. The electrochemical parameters are indicated in **Table 4**.

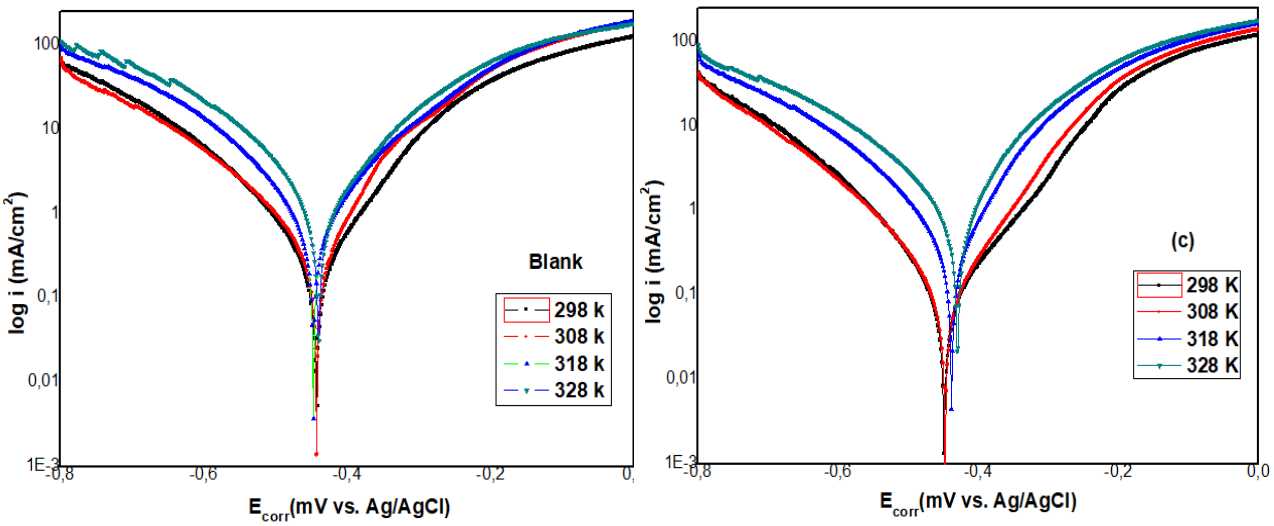

Figure 9. Polarization curves of carbon steel in 1 M HCl solution in the absence (Blank) and presence (c) of the inhibitor (3c) 10^{-3}M at 298, 308, 318 and 328K

Table 4 Potentiodynamic polarization parameters for the corrosion of carbon steel in 1 M HCl solution in the absence and presence of the inhibitor (**3c**) 10^{-3}M at 298, 308, 318 and 328K

T(K)	C (M)	E_{corr}(mVvs.Ag/AgCl)	i_{corr}(mA/cm^2)	βc (mV/dec)	βa (mV/dec)	EI (%)
298	0	-443.375	351.381	130.9	108.6	-
	10^{-3}	-442.345	68.135	97.6	93.1	80.60
308	0	-442.774	394.411	133.4	93	
	10^{-3}	-447.494	109.717	114.6	93.1	72.18
318	0	-447.391	1 072.51	143.3	139.2	-
	10^{-3}	-438.022	388.342	118.5	90.2	63.79
328	0	-439.945	1 597.45	139.3	140.9	-
	10^{-3}	-429.566	818.166	128.4	90.5	48.78

According to these results, it is observed that the inhibition efficiency decreases with increasing temperature. This is due to the desorption of inhibitor molecules attached to the steel surface, thus inducing the dissolution of the steel (Ouici *et al.* 2017). therefore, it can be assumed that the bonds between the inhibitors and the steel surface are of low energy which promotes physical adsorption (Oguzie *et al.* 2004).

3.5 Thermodynamic parameters

Concerning the thermodynamic parameters, studies have shown that the enthalpy (ΔHa), entropy (ΔSa) and activation energies (Ea), provide information about the adsorption mechanism of inhibitors on the metal surface (Rajamohan *et al.* 2022). These parameters are calculated by the following Arrhenius relationships (15) and (16):

$$i_{corr}=A\exp\left(\frac{-E_a}{RT}\right) \qquad (15)$$

$$i_{corr}=\frac{RT}{Nh}\exp\left(\frac{\Delta S_a}{R}\right)\exp\left(\frac{-\Delta H_a}{RT}\right) \qquad (16)$$

From the plot of ($\ln i_{corr}$) vs (1/T) (**Erreur ! Source du renvoi introuvable.**(B)), we deduce the value of the energy (Ea) (Arrhenius slope). The energies ΔHa and ΔSa are calculated from the slope (-ΔHa/R) and the ordinate of origin (ln R/Nh + ΔSa/R) of the plot of $\ln(i_{corr}/T)$ vs (1/T) (**Erreur ! Source du renvoi introuvable.0**(A)), respectively. The calculated thermodynamic parameters are presented in **Table 5**.

These results show that the inhibitor solution with the metal has activation energy (Ea) of the order of 70.66 kJ/mol, which is higher than that of the Blank solution with the metal (44.78 kJ/mol), indicating that the presence of an inhibitor resulted in a larger energy barrier (Alamiery 2021), and assert the ability of the inhibitor molecules to adsorb onto the surface of the carbon steel, creating a protective barrier (Tebbji *et al.* 2007). The positive value of ΔHa shows that the dissolution process of the metal is endothermic (Khoshsang and Ghaffarinejad 2022). The value of the activation entropy (ΔSa) obtained is negative in the absence of the inhibitor, and positive in the presence of the inhibitor, this is explained by an increase in molecular disorder after the addition of the inhibitor (**3c**) (Laabaissi *et al.* 2020).

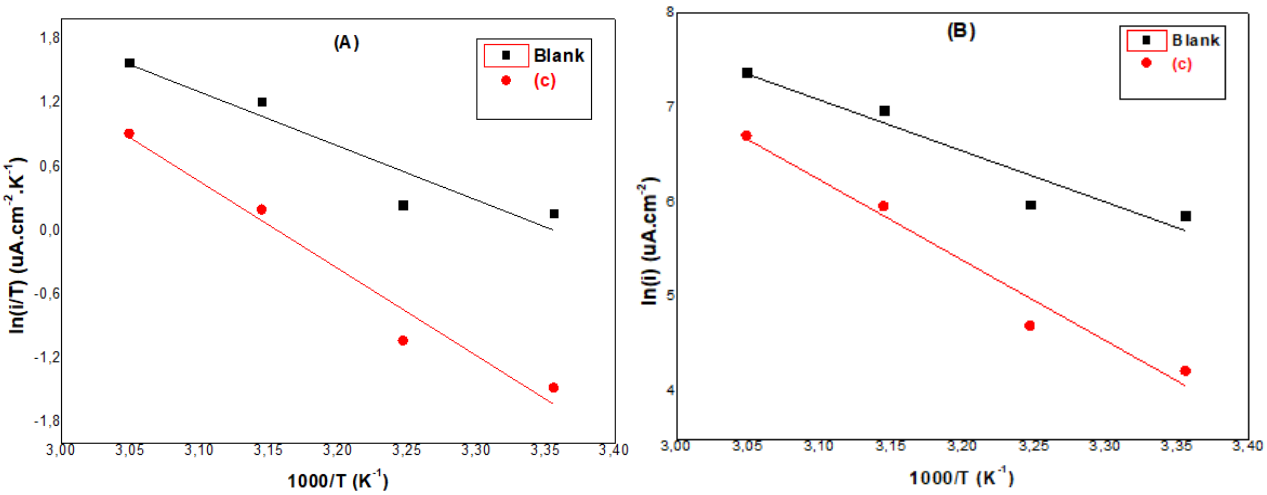

Figure 10. Variation of ln i_{corr}/T as a function of 1/T (A) and ln i_{corr} as a function of 1/T (B) of steel in 1M HCl with (Blank) and without the addition of **3c** (c) at optimum concentration 10^{-3} M

Table 5 Activation parameters for carbon steel in 1M HCl without and with inhibitor **3c** at 10^{-3}M

Inhibitor	Ea (kJ/mol)	ΔHa (Kj/mol)	ΔSa (J/K mol)
Blank	44.78	42.23	-56.17
3c	70.66	68.05	16.95

3.6. Surface analyses SEM/EDX

Morphological analysis is used to obtain information on the effect of corrosion on the steel surface. **Erreur ! Source du renvoi introuvable.1** represents the surface morphology of the steel after immersion in the 1 M HCl medium with and without 10^{-3} M of the studied compounds for 20 h and at a temperature of 298 K. These micrographs show that the surface was severely attacked by the corrosive solution without the presence of an inhibitor, resulting in damage (Kharbach *et al.* 2017).

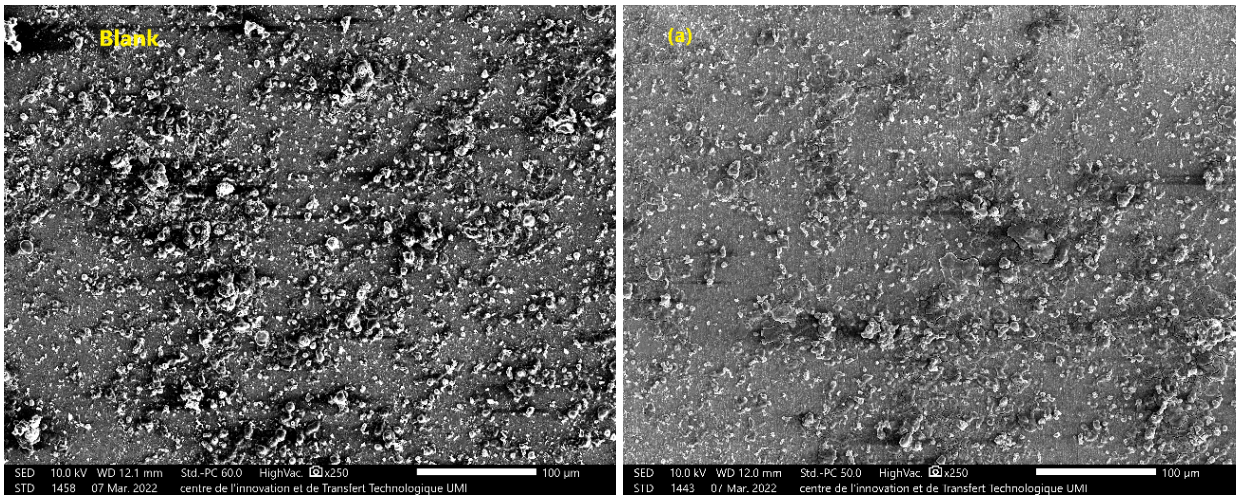

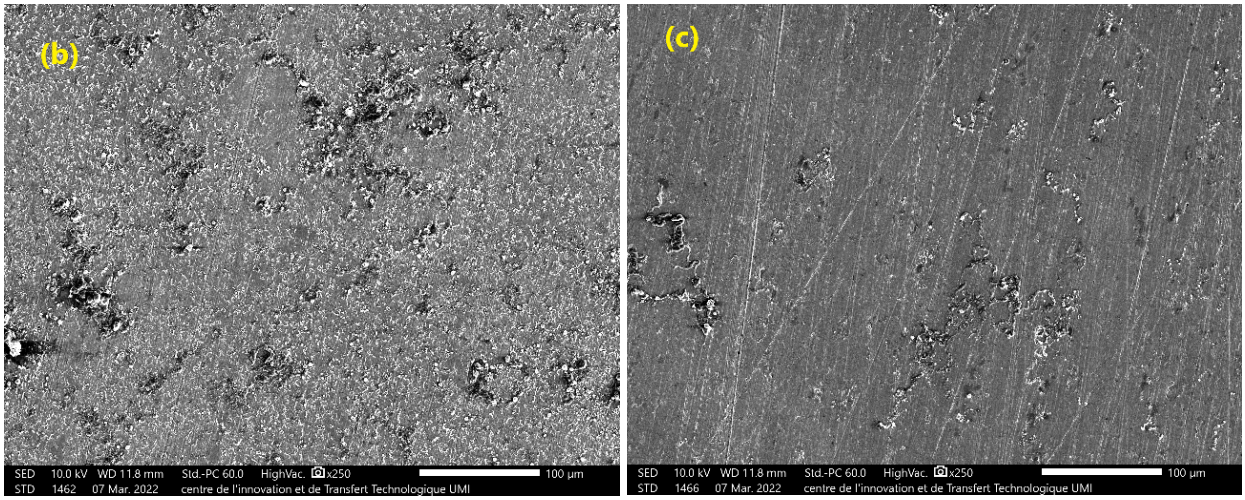

Figure 11. SEM images of steel surface after 20 h immersion in 1 M HCl without inhibitor (blank), (a) with 10^{-3} M of **3a**, (b) with 10^{-3} M of **3b**, (c) with 10^{-3} M of **3c**

In the presence of 10^{-3}M of each inhibitor, the electrode surface becomes smooth, and we also note the disappearance of damage brought on by the corrosive solution, particularly for compound **3c** confirming the hay protective effect of this inhibitor on the electrode surface compared to compounds **3a** and **3b**. The surface of the carbon steel was also analyzed by EDX. The results obtained (Erreur ! Source du renvoi introuvable.**2**) showed that, in the presence of the inhibitors, the percentage of iron has increased due to the decrease in the extent of acid corrosion, thus the increase of carbon peak, which can be explained by the formation of a layer of carbon-based molecules on the surface of the steel (Mistry *et al.* 2012). Due to the creation of the Fe-inhibitor interaction on the steel surface, which creates a protective coating on the metal surface, the percentage of oxygen is always decreased in the presence of the inhibitor.

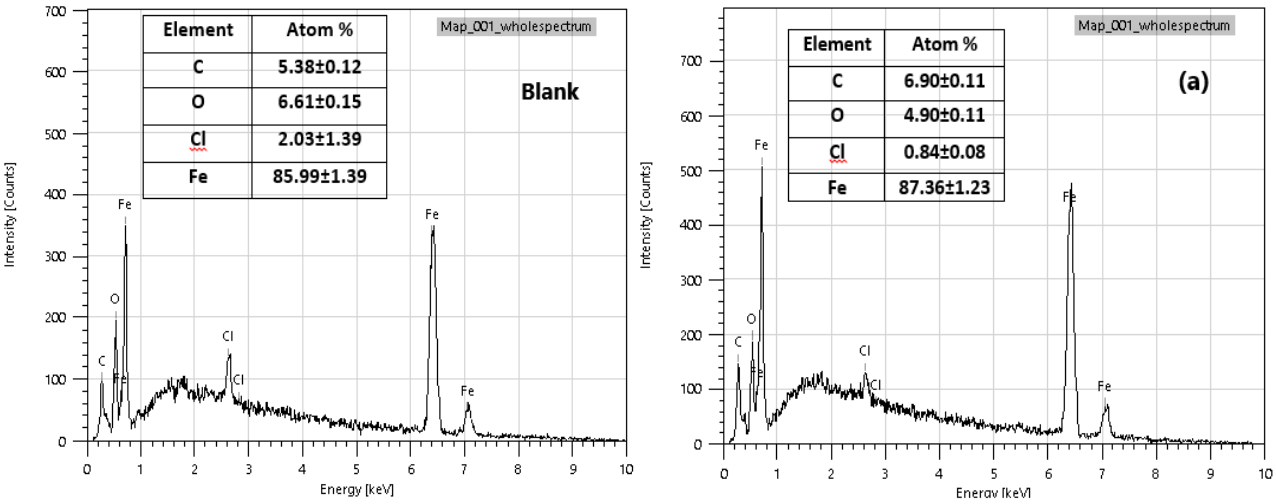

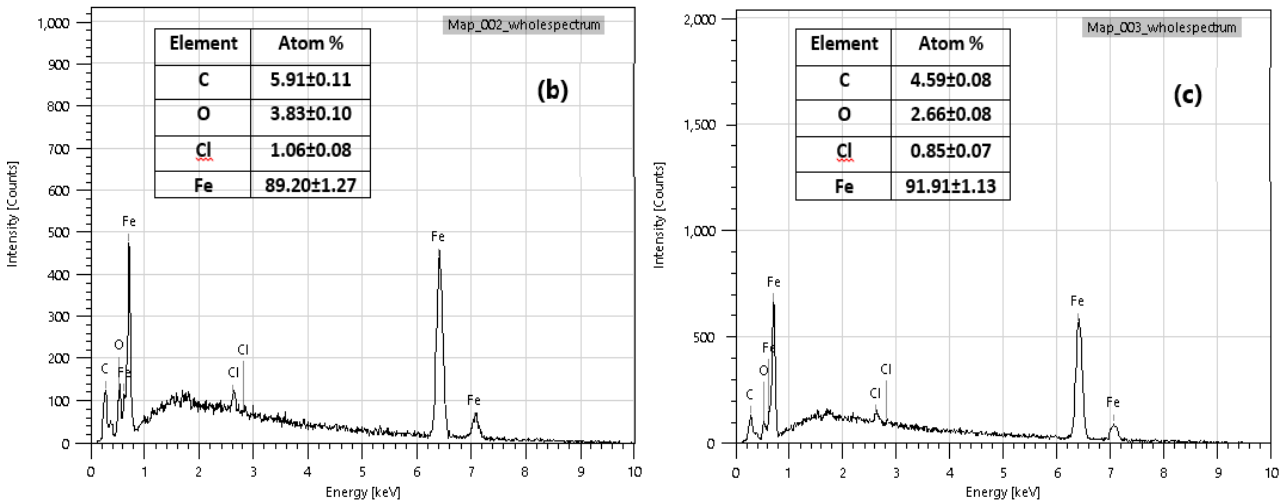

Figure 12. EDX data of steel surfaces after 20 h immersion in 1 M HCl without inhibitor (blank), (a) with 10^{-3} M of **3a**, (b) with 10^{-3} M of **3b**, (c) with 10^{-3} M of **3c.**

3.7. Quantum chemical calculations

Quantum chemical calculations were used in the corrosion domain to predict or confirm the experimental results. The optimized structure and Mulliken atomic charges of inhibitors **3a**, **3b** and **3c,** are illustrated in **Fig. 13**. Electrostatic potential map (ESP), LUMO and HOMO, are shown in **Fig. 14** and the calculated molecular and electronic parameters concerning the behavior of the inhibitors were listed in **Table 6** and **Table 7**. **Erreur ! Source du renvoi introuvable.13** shows that the partial charges of the oxygen atoms in red, as well as of some carbons of the inhibitor compounds, have relatively negative values, then these atoms can be described as the centers of adsorption. In general, heteroatoms act as electron donors to the orbitals of metal atoms (Bahron *et al.* 2021). These heteroatoms contribute to the success of the adsorption process on the steel surface.

Erreur ! Source du renvoi introuvable.**14** shows the ESP of the three optimal molecules **3a**, **3b** and **3c**, this figure shows the charge distribution, where the red colors signify the maximum negative region (nucleophilic center) and the blue colors represent the most positive regions (electrophilic center) (Ramalingam *et al.* 2011). For the three inhibitors, the negative regions are mainly found on the oxygen atoms of the lactone ring and the oxygen atom of the methoxy group of **3c**. The inhibitory activity of a compound is related to its molecular boundary orbitals, the LUMO and HOMO, the values of the energies of LUMO (E_{LUMO}) and HOMO (E_{HOMO}) indicate the capacity of a molecule to receive or give electrons (Tan *et al.* 2017).

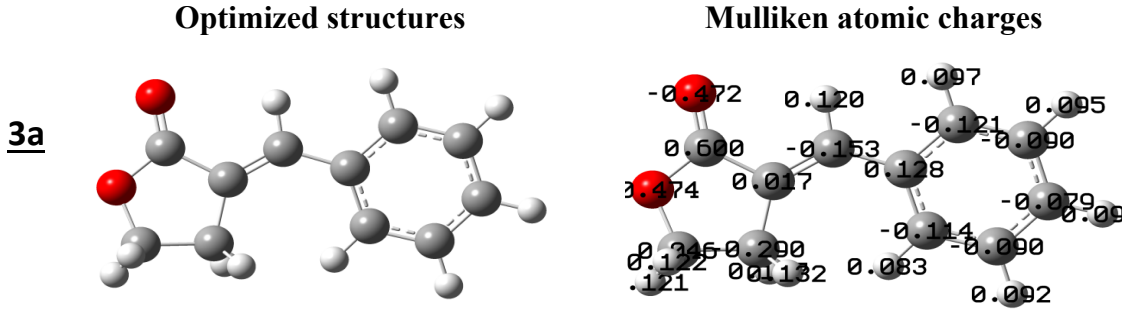

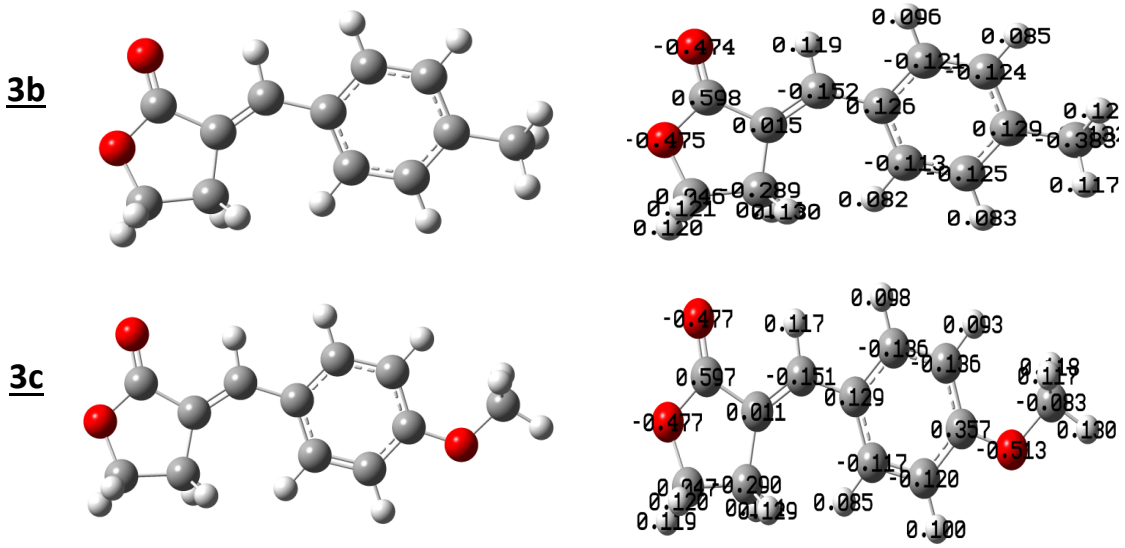

Figure 13. Optimized structure and Mulliken's charges of inhibitors **3a**, **3b** and **3c**

According to the literature, the low E_{LUMO} values illustrate that the inhibitor tends to accept electrons (Tan *et al.* 2019). Whereas, in the case of high E_{HOMO} the inhibitors have a strong tendency to give up electrons (Mourya *et al.* 2013). Also, the effectiveness of a corrosion inhibitor depends on the energy gap (ΔEg) (Asadi et al. 2019). Lower values of ΔEg generally lead to greater adsorption of the inhibitor on the metal surface (Qiang *et al.* 2017). In our study, based on the E_{HOMO} and ΔEg values (**Table 6**), the efficacy of the three inhibitors is ranked in the following order: **3c** > **3b** > **3a**, which are in agreement with the experimental results. **Table 7**, shows the values of the different electronic parameters, the values of the dipole moment of the inhibitors **3a**, **3b** and **3c** are 5.20, 5.69 and 5.81 Debye, respectively. Several authors have deduced that for high values of the dipole moment, The inhibitor's dipole-dipole interactions with the metal surface are very important (Qiang *et al.* 2016 ; Qiang et al. 2018). In our study, the order of these values (5.81 > 5.69 > 5.20) is in excellent accordance with the experimentally determined inhibitory efficiencies (**3c** > **3b** > **3a**).

Moreover, the smallest electronegativity value (χ), can be associated with a stronger tendency to donate electrons by a molecule to the steel surface and vice versa (Palaniappan *et al.* 2020). On the other hand, a compound with a low value of hardness (η) and a high value of softness (S) is associated with a strong interaction with the metal, then a high inhibition efficiency (Sayin and Karakaş 2013). The empirically determined order of experimentally inhibition efficiencies (**3c** > **3b** > **3a**) is confirmed by these obtained values of (χ), (η), and (S). The literature shows that, if the value of the fraction of electron transferred (ΔN) from inhibitors to the lower metal is 3.6, inhibition efficiency improves with increasing ΔN (Lukovits *et al.* 2001). In our case, the values of ΔN are 0.1582, 0.1920 and 0.2564 for **3a**, **3b** and **3c** respectively, which confirms the best efficiency for **3c** followed by **3b** and by **3a**.

HOMO **LUMO** **ESP**

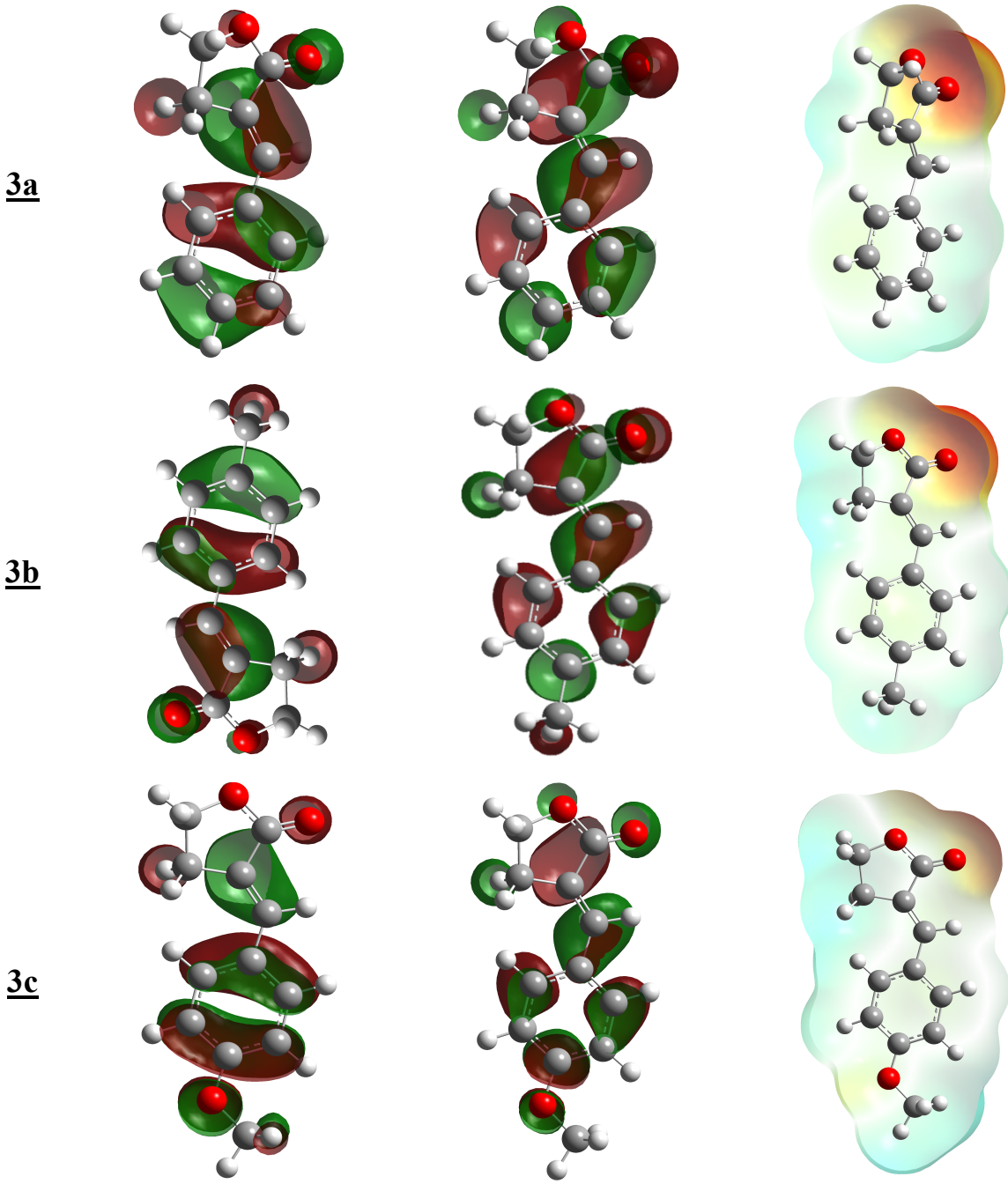

Figure 14. HOMO, LUMO and ESP of inhibitors **3a**, **3b**, and **3c**

Table 6 Total energy, E_{HOMO}, E_{LUMO} and the energetic gap of inhibitors **3a**, **3b**, and **3c**

Inhibitor	Total energy	E_{HOMO} (eV)	E_{LUMO} (eV)	ΔEg (eV)
3a	-575.6528	-6.3952	-1.7862	4.6091
3b	-614.9741	-6.2077	-1.7023	4.5054
3c	-690.1796	-5.8728	-1.5516	4.3212

Table 7 Molecular and electronic parameters of inhibitors **3a**, **3b** and **3c**

Inhibitor	dipolar moment	Polarisability	I	A	χ	μ	η	S	ω	ΔN	ΔE
3a	5.20	125.05	6.39	1.79	4.09	-4.09	2.30	0.434	3.63	0.158	0.058
3b	5.69	141.26	6.21	1.70	3.95	-3.95	2.25	0.444	3.47	0.192	0.083
3c	5.81	149.64	5.87	1.55	3.71	-3.71	2.16	0.463	3.19	0.256	0.142

Conclusion

This work focused on the synthesis of a series of dipolarophiles (**3a**, **3b** and **3c**) of alkene nature with the two carbons forming the double bond differently substituted by a microwave oven technique. Additionally, these compounds' abilities to prevent corrosion on steel in a solution of 1 M HCl were investigated using electrochemical techniques and theoretical calculations. The next conclusions were reached:

(1) These olefins were synthesized in good yields, 90% for **3a**, 92% for **3b**, and 90% for **3c**.

(2) The synthetic approach based on the microwave oven technique in a dry medium is effective for the synthesis of these compounds.

(3) The structures of the dipolarophiles were identified using ^{1}H, ^{13}C NMR and IR spectroscopic analyses. The structure of compound **3b** was confirmed by using RDX.

(4) These compounds act as effective corrosion inhibitors with maximum efficiencies of 80.61%, 76.59 and 74.66% for inhibitors **3c**, **3b**, and **3a** respectively, at a concentration of 10^{-3}M.

(5) The tested inhibitors were adsorbed at the interface of the carbon steel/HCl following the Langmuir isothermal model. The free energy values showed both chemical and physical adsorption of these inhibitors on the steel interface, with physical adsorption predominating.

(6) SEM coupled with EDX analysis confirmed the protection of the steel surface by these inhibitors.

(7) The results obtained from the DFT investigation show good agreement between the calculated theoretical parameters and the experimental data.

(8) Experimental results and quantum chemical calculations show that **3c** is the best inhibitor followed by **3b** and **3a**.

Disclosure statement: *Conflict of Interest:* The authors declare that there are no conflicts of interest.
Compliance with Ethical Standards: This article does not contain any studies involving human or animal subjects.

References

Abdul Rahiman A. F. S., Sethumanickam S, (2017) Corrosion inhibition, adsorption and thermodynamic properties of poly(vinyl alcohol-cysteine) in molar HCl, *Arab J Chem*, 10, S3358–S3366. doi: 10.1016/j.arabjc.2014.01.016

Ait Chikh Z., Chebabe D., Dermaj A., Hajjaji N., Srhiri A., Montemor M. F., Ferreira M. G. S., Bastos A. C., (2005) Electrochemical and analytical study of corrosion inhibition on carbon steel in HCl medium by 1,12-bis(1,2,4-triazolyl) dodecane, *Corros. Sci,* 47, 447–459. doi: 10.1016/j.corsci.2004.05.028

Alamiery A., (2021) Corrosion inhibition effect of 2-N-phenylamino-5-(3-phenyl-3-oxo-1-propyl)-1,3,4-oxadiazole on mild steel in 1 M hydrochloric acid medium: Insight from gravimetric and DFT investigations, *Mater Sci Energy Technol*, 4, 398–406. doi: 10.1016/j.mset.2021.09.002

Ansari K. R., Quraishi M. A., Singh A., (2014) Schiff's base of pyridyl substituted triazoles as new and effective corrosion inhibitors for mild steel in hydrochloric acid solution, *Corros Sci*, 79, 5–15. doi: 10.1016/j.corsci.2013.10.009

Anusuya N., Saranya J., Sounthari P., Zarrouk A., Chitra S., (2017) Corrosion inhibition and adsorption behaviour of some bis-pyrimidine derivatives on mild steel in acidic medium, J Mol Liq, 225, 406–417. doi: 10.1016/j.molliq.2016.11.015

Asadi N., Ramezanzadeh M., Bahlakeh G., Ramezanzadeh B., (2019) Utilizing Lemon Balm extract as an effective green corrosion inhibitor for mild steel in 1M HCl solution: A detailed experimental, molecular dynamics, Monte Carlo and quantum mechanics study, *J Taiwan Inst Chem Eng*, 95, 252–272. doi: 10.1016/j.jtice.2018.07.011

Bahron H., Ghani A. A., Anouar E.H., Embong Z., Alharthi A.I., Harun M.K., Alias Y., (2021) Adsorption, electrochemistry, DFT and inhibitive effect of imines derived from tribulin on corrosion of mild steel in 1 M HCl, *J Mol Struct*, 1235, 130206. doi: 10.1016/j.molstruc.2021.130206

Bayol E., Gurten A., Dursun M., Kayakirilmaz K., (2008) Adsorption Behavior and Inhibition Corrosion Effect of Sodium Carboxymethyl Cellulose on Mild Steel in Acidic Medium, *Acta Phys-Chim Sin*,24, 2236–2243. doi: 10.1016/S1872-1508(08)60085-6

Bouanis M., Tourabi M., Nyassi A., Zarrouk A., Jama C., Bentiss F., (2016) Corrosion inhibition performance of 2,5-bis(4-dimethylaminophenyl)-1,3,4-oxadiazole for carbon steel in HCl solution: Gravimetric, electrochemical and XPS studies, *Appl Surf Sci*, 389, 952–966, doi: 10.1016/j.apsusc.2016.07.115

Bouklah M., Ouassini A., Hammouti B., El Idrissi A. (2006) Corrosion inhibition of steel in sulphuric acid by pyrrolidine derivatives, *Applied surface science* 252 (6), 2178-2185

Chebabe D., Ait Chikh Z., Dermaj A., Rhattas K., Jazouli T., Hajjaji N., El Mdari F., Srhiri A., (2004) Synthesis of bolaamphiphile surfactants and their inhibitive effect on carbon steel corrosion in hydrochloric acid medium, *Corros Sci,* 46, 2701–2713. doi: 10.1016/j.corsci.2004.03.016

Častulík J., Marek J., Mazala C., (2001) Synthesis of spiropyrrolidines and spiropyrrolizidines by 1,3-dipolar cycloadditions of azomethine ylides to substituted α-methylene-γ-lactones. *Tetrahedron,* 57, 8339-8347. doi: 10.1016/S0040-4020(01)00807-9

Dagdag O., El Harfi A., Cherkaoui O., Safi Z., Wazzan N., Guo L., Akpan E. D., Verma C., Ebenso E. E., Jalgham RTT, (2019) Rheological, electrochemical, surface, DFT and molecular dynamics simulation studies on the anticorrosive properties of new epoxy monomer compound for steel in 1 M HCl solution, *RSC Adv*, 9, 4454–4462. doi: 10.1039/C8RA09446B

de Souza F. S., Spinelli A., (2009) Caffeic acid as a green corrosion inhibitor for mild steel, *Corros Sci,* 51, 642–649. doi: 10.1016/j.corsci.2008.12.013

de Souza V. A., da Silva R., Pereira A. C., Royo V de A., Saraiva J., Montanheiro M., de Souza G. H. B., da Silva Filho A. A., Grando M. D., Donate P. M., Bastos J. K., Albuquerque S., e Silva M. L. A., (2005) Trypanocidal activity of (−)-cubebin derivatives against free amastigote forms of Trypanosoma cruzi, *Bioorg Med Chem Lett*, 15, 303–307. doi: 10.1016/j.bmcl.2004.10.079

Eid AM., Shaaban S., Shalabi K., (2020) Tetrazole-based organoselenium bi-functionalized corrosion inhibitors during oil well acidizing: Experimental, computational studies, and SRB bioassay, *J Mol Liq*, 298, 111980. doi: 10.1016/j.molliq.2019.111980

Farahati R., Mousavi-Khoshdel S. M., Ghaffarinejad A., Behzadi H., (2020) Experimental and computational study of penicillamine drug and cysteine as water-soluble green corrosion inhibitors of mild steel, *Prog Org Coat*, 142, 105567. doi: 10.1016/j.porgcoat.2020.105567

Fateh A., Aliofkhazraei M., Rezvanian A. R., (2020) Review of corrosive environments for copper and its corrosion inhibitors, *Arab J Chem*, 13, 481–544. doi: 10.1016/j.arabjc.2017.05.021

Fernine Y., Salim R., Arrousse N., Haldhar R., El Hajjaji F., Kim S-C., Ebn Touhami M., Taleb M., (2022) Anti-corrosion performance of Ocimum basilicum seed extract as environmental friendly inhibitors for

mild steel in HCl solution: Evaluations of electrochemical, EDX, DFT and Monte Carlo, *J. Mol. Liq.*, 355, 118867. doi: 10.1016/j.molliq.2022.118867

Gao L., Peng S., Huang X., Gong Z., (2020) A combined experimental and theoretical study of papain as a biological eco-friendly inhibitor for copper corrosion in H2SO4 medium, *Appl. Surf. Sci.,* 511, 145446. doi: 10.1016/j.apsusc.2020.145446

Hafez B., Mokhtari M., Elmsellem H., Steli H., (2019) Environmentally friendly inhibitor of the corrosion of mild steel: Commercial oil of Eucalyptus, *Int. J. Corros. Scale Inhib*, 8, 573–585. doi: 10.17675/2305-6894-2019- 8-3-8

He J., Li Q., Li X., An J., Chen G., Zhao L., Li W, (2020) Insight into the anti-corrosion mechanism of 2-aminobenzenethiol as the inhibitor for copper in acid environment, *J. Mol. Liq.*, 320,114494. doi: 10.1016/j.molliq.2020.114494

Huang Y., Zhu Q., Zhou Z., Zhou Y., Cang H., Tang Y., (2022) Corrosion behavior of low-alloy steel in tidal zone: A simulated investigation. *Mater. Today. Commun.*, 31, 103704. doi: 10.1016/j.mtcomm.2022.103704

K T L, Thimmakondu VS., S N, R N., (2021) Corrosion inhibitive evaluation and DFT studies of 2-(Furan-2-yl)-4,5-diphenyl-1H-imidazole on mild steel at 1.0M HCl, *J Indian Chem Soc*, 98, 100121. doi: 10.1016/j.jics.2021.100121

Karthikaiselvi R., Subhashini S., (2014) Study of adsorption properties and inhibition of mild steel corrosion in hydrochloric acid media by water soluble composite poly (vinyl alcohol-omethoxy aniline), *J Assoc Arab Univ Basic Appl Sci*, 16, 74–82. doi: 10.1016/j.jaubas.2013.06.002

Kharbach Y., Qachchachi F. Z., Haoudi A., Tourabi M., Zarrouk A., Jama C., Olasunkanmi L. O., Ebenso E. E., Bentiss F., (2017) Anticorrosion performance of three newly synthesized isatin derivatives on carbon steel in hydrochloric acid pickling environment: Electrochemical, surface and theoretical studies, *J Mol Liq*, 246, 302–316. doi: 10.1016/j.molliq.2017.09.057

Khoshsang H., Ghaffarinejad A., (2022) Sunflower petals extract as a green, eco-friendly and effective corrosion bioinhibitor for carbon steel in 1M HCl solution. Chem Data Collect, 37, 100799. doi: 10.1016/j.cdc.2021.100799

Kovačević N., Kokalj A., (2011) DFT Study of Interaction of Azoles with Cu (111) and Al (111) Surfaces: Role of Azole Nitrogen Atoms and Dipole–Dipole Interactions, *J Phys Chem C*, 115, 24189–24197. doi: 10.1021/jp207076w

Laabaissi T., Benhiba F., Missioui M., Rouifi Z., Rbaa M., Oudda H., Ramli Y., Guenbour A., Warad I., Zarrouk A., (2020) Coupling of chemical, electrochemical and theoretical approach to study the corrosion inhibition of mild steel by new quinoxaline compounds in 1 M HCl, *Heliyon,* 6, e03939. doi: 10.1016/j.heliyon.2020.e03939

Lgaz H., Salghi R., Masroor S., Kim S-H., Chang K., Kim S. Y., Yang Y-J., Chung I-M. (2020) Assessing corrosion inhibition characteristics of hydrazone derivatives on mild steel in HCl: Insights from electronic-scale DFT and atomic-scale molecular dynamics, *Journal of Molecular Liquids,* 308, 112998, ISSN 0167-7322, https://doi.org/10.1016/j.molliq.2020.112998

Lukovits I., Kálmán E., Zucchi F., (2001) Corrosion Inhibitors—Correlation between Electronic Structure and Efficiency, *corrosion*, 57, 3–8. doi: 10.5006/1.3290328

Ma Q., Qi S., He X., Tang Y., Lu G., (2017) 1,2,3-Triazole derivatives as corrosion inhibitors for mild steel in acidic medium: Experimental and computational chemistry studies, *Corros Sci*, 129, 91–101. doi: 10.1016/j.corsci.2017.09.025

Mehl F., Bombarda I., Vanthuyne N., Faure R., Gaydou E. M., (2010) Hemisynthesis and odour properties of δ-hydroxy-γ-lactones and precursors derived from linalool, *Food Chem,* 121, 98–104. doi: 10.1016/j.foodchem.2009.12.010

Mistry B.M., Patel N. S., Sahoo S., Jauhari S., (2012) Experimental and quantum chemical studies on corrosion inhibition performance of quinoline derivatives for MS in 1N HCl, *Bull Mater Sci,* 35, 459–469. doi: 10.1007/s12034-012-0308-4

Mobin M., Parveen M., Huda., Aslam R., (2022) Effect of different additives, temperature, and immersion time on the inhibition behavior of L-valine for mild steel corrosion in 5% HCl solution, *J Phys Chem Solids*, 161, 110422. doi: 10.1016/j.jpcs.2021.110422

Mourya P., Banerjee S., Rastogi R. B., Singh M.M., (2013) Inhibition of Mild Steel Corrosion in Hydrochloric and Sulfuric Acid Media Using a Thiosemicarbazone Derivative, *Ind Eng Chem Res*, 52, 12733–12747. https://doi.org/10.1021/ie4012497

Oguzie E. E., Unaegbu C., Ogukwe C. N., Okolue B. N., Onuchukwu A. I., (2004) Inhibition of mild steel corrosion in sulphuric acid using indigo dye and synergistic halide additives, *Mater Chem Phys*, 84, 363–368. doi: 10.1016/j.matchemphys.2003.11.027

Olasunkanmi L.O., Kabanda M.M., Ebenso E.E., (2016) Quinoxaline derivatives as corrosion inhibitors for mild steel in hydrochloric acid medium: Electrochemical and quantum chemical studies. *Phys E Low-Dimens Syst Nanostructures*, 76, 109–126. doi: 10.1016/j.physe.2015.10.005

Ouici H., Tourabi M., Benali O., Selles C., Jama C., Zarrouk A., Bentiss F., (2017) Adsorption and corrosion inhibition properties of 5-amino 1,3,4-thiadiazole-2-thiol on the mild steel in hydrochloric acid medium: Thermodynamic, surface and electrochemical studies, *J Electroanal Chem*, 803, 125–134. doi: 10.1016/j.jelechem.2017.09.018

Palaniappan N., Cole I. S., Kuznetsov A. E., (2020) Experimental and computational studies of graphene oxide covalently functionalized by octylamine: electrochemical stability, hydrogen evolution, and corrosion inhibition of the AZ13 Mg alloy in 3.5% NaCl, *RSC Adv*, 10, 11426–11434. doi: 10.1039/C9RA10702A

Qiang Y., Fu S., Zhang S., Chen S., Zou X., (2018) Designing and fabricating of single and double alkyl-chain indazole derivatives self-assembled monolayer for corrosion inhibition of copper, *Corros Sci*, 140,111–121. doi: 10.1016/j.corsci.2018.06.012

Qiang Y., Zhang S., Guo L., Zhang X., Xiang B., Chen S., (2017) Experimental and theoretical studies of four allyl imidazolium-based ionic liquids as green inhibitors for copper corrosion in sulfuric acid, *Corros Sci*, 119, 68–78. doi: 10.1016/j.corsci.2017.02.021

Qiang Y., Zhang S., Xu S., Li W., (2016) Experimental and theoretical studies on the corrosion inhibition of copper by two indazole derivatives in 3.0% NaCl solution, *J Colloid Interface Sci,* 472, 52–59. doi: 10.1016/j.jcis.2016.03.023

Rajamohan N., Zahir Said Al Shibli F. S., Rajasimman M., Vasseghian Y., (2022) Eco-friendly biomass from Ziziphus spina-christi for protection of carbon steel in acidic conditions – Parameter effects and corrosion mechanism studies, *Chemosphere*, 291, 132756. doi: 10.1016/j.chemosphere.2021.132756

Ramalingam S., David Suresh Babu P., Periandy S., Fereyduni E., (2011) Vibrational investigation, molecular orbital studies and molecular electrostatic potential map analysis on 3-chlorobenzoic acid using hybrid computational calculations. *Spectrochim Acta A Mol Biomol Spectrosc*, 84, 210–220. doi: 10.1016/j.saa.2011.09.030

Ramezanzadeh B., Arman S. Y., Mehdipour M., Markhali B. P., (2014) Analysis of electrochemical noise (ECN) data in time and frequency domain for comparison corrosion inhibition of some azole compounds on Cu in 1.0M H2SO4 solution, *Appl Surf Sci*, 289, 129–140. doi: 10.1016/j.apsusc.2013.10.119

Rbaa M., Galai M., Benhiba F., Obot I. B., Oudda H., Ebn Touhami M., Lakhrissi B., Zarrouk A., (2019) Synthesis and investigation of quinazoline derivatives based on 8-hydroxyquinoline as corrosion inhibitors for mild steel in acidic environment: experimental and theoretical studies, *Ionics*, 25, 3473–3491. doi: 10.1007/s11581-018-2817-7

Reutrakul V., Krachangchaeng C., Tuchinda P., Pohmakotr M., Jaipetch T., Yoosook C., Kasisit J., Sophasan S., Sujarit K., Santisuk T., (2004) Cytotoxic and anti-HIV-1 constituents from leaves and twigs of Gardenia tubifera, *Tetrahedron*, 60, 1517–1523. doi: 10.1016/j.tet.2003.12.010

Romagnoli R., Baraldi P. G., Carrion M. D., Cara C. L., Preti D., Fruttarolo F., Pavani M. G., Tabrizi M. A., Tolomeo M., Grimaudo S., Di Cristina A., Balzarini J., Hadfield J. A., Brancale A., Hamel E., (2007) Synthesis and Biological Evaluation of 2- and 3-Aminobenzo[*b*]thiophene Derivatives as Antimitotic Agents and Inhibitors of Tubulin Polymerization, *J. Med. Chem*. 50, 2273–2277. doi: 10.1021/jm070050f

Sayin K., Karakaş D., (2013) Quantum chemical studies on the some inorganic corrosion inhibitors, *Corros Sci*, 77:37–45. doi: 10.1016/j.corsci.2013.07.023

Solmaz R. 2014. Investigation of adsorption and corrosion inhibition of mild steel in hydrochloric acid solution by 5-(4-Dimethylaminobenzylidene)rhodanine. *Corros Sci.* 79, 169–176. doi: 10.1016/j.corsci.2013.11.001

Tambe A., Gadhave A., Pathare A., Shirole G., (2021) Novel Pumice@SO_3H catalyzed efficient synthesis of 2,4,5-triarylimidazoles and acridine-1,8-diones under microwave assisted solvent-free path. *Sustain Chem Pharm*, 22, 100485. doi: 10.1016/j.scp.2021.100485

Tan B., Zhang S., Liu H., Guo Y., Qiang Y., Li W., Guo L., Xu C., Chen S., (2019) Corrosion inhibition of X65 steel in sulfuric acid by two food flavorants 2-isobutylthiazole and 1-(1,3-Thiazol-2-yl) ethanone as the green environmental corrosion inhibitors: Combination of experimental and theoretical researches. *J Colloid Interface Sci*, 538, 519–529. doi: 10.1016/j.jcis.2018.12.020

Tan B., Zhang S., Qiang Y., Feng L., Liao C., Xu Y., Chen S., (2017) Investigation of the inhibition effect of Montelukast Sodium on the copper corrosion in 0.5 mol/L H_2SO_4, *J Mol Liq,* 248, 902–910. doi: 10.1016/j.molliq.2017.10.111

Tebbji K., Faska N., Tounsi A., Oudda H., Benkaddour M., Hammouti B., (2007) The effect of some lactones as inhibitors for the corrosion of mild steel in 1M hydrochloric acid, *Mater Chem Phys*, 106, 260–267. doi: 10.1016/j.matchemphys.2007.05.046

Thari F. Z., Tachallait H., El Alaoui N-E., Talha A., Arshad S., Álvarez E., Karrouchi K., Bougrin K., (2020) Ultrasound-assisted one-pot green synthesis of new N- substituted-5-arylidene-thiazolidine-2,4-dione-isoxazoline derivatives using NaCl/Oxone/Na_3PO_4 in aqueous media, *Ultrason Sonochem*, 68, 105222. doi: 10.1016/j.ultsonch.2020.105222

Titi A., Mechbal N., El Guerraf A., El Azzouzi M., Touzani R., Hammouti B., Chung I-M., Lgaz H. (2018) Experimental and theoretical studies on inhibition of carbon steel corrosion by 1,5-diaminonaphthalene, *J. Bio- and Tribo-Corrosion*, 4(2), 22, https://doi.org/10.1007/s40735-018-0140-5

Umar Y., (2022) Experimental (FT-IR, FT-Raman, and NMR) and DFT studies of the structures and spectral properties of diphenylcarbazone and diphenylthiocarbazone, *J Mol Struct*, 1264, 133230. doi: 10.1016/j.molstruc.2022.133230

Wang J., Liu J., Liu Q., Chong Y., (2021) The inhibition performance of heterocyclic compounds on Q235 steel in methanol/formic acid medium: Experimental and theory, *J Mol Struct*, 343, 117663. doi: 10.1016/j.molliq.2021.117663

Annex

(Supplementary Data)

Spectroscopic data of synthesized olefin derivatives

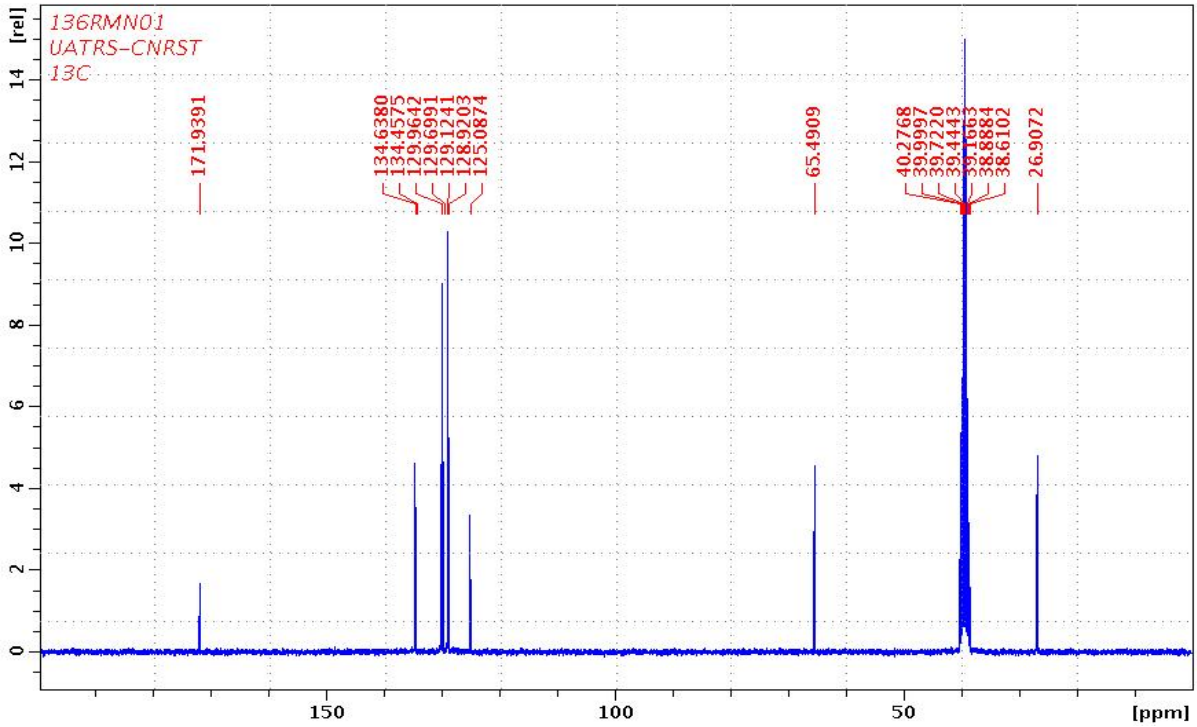

Figure S1: ^{13}C-NMR spectrum of α-benzelidenyl- γ-butyrolactone (**3a**)

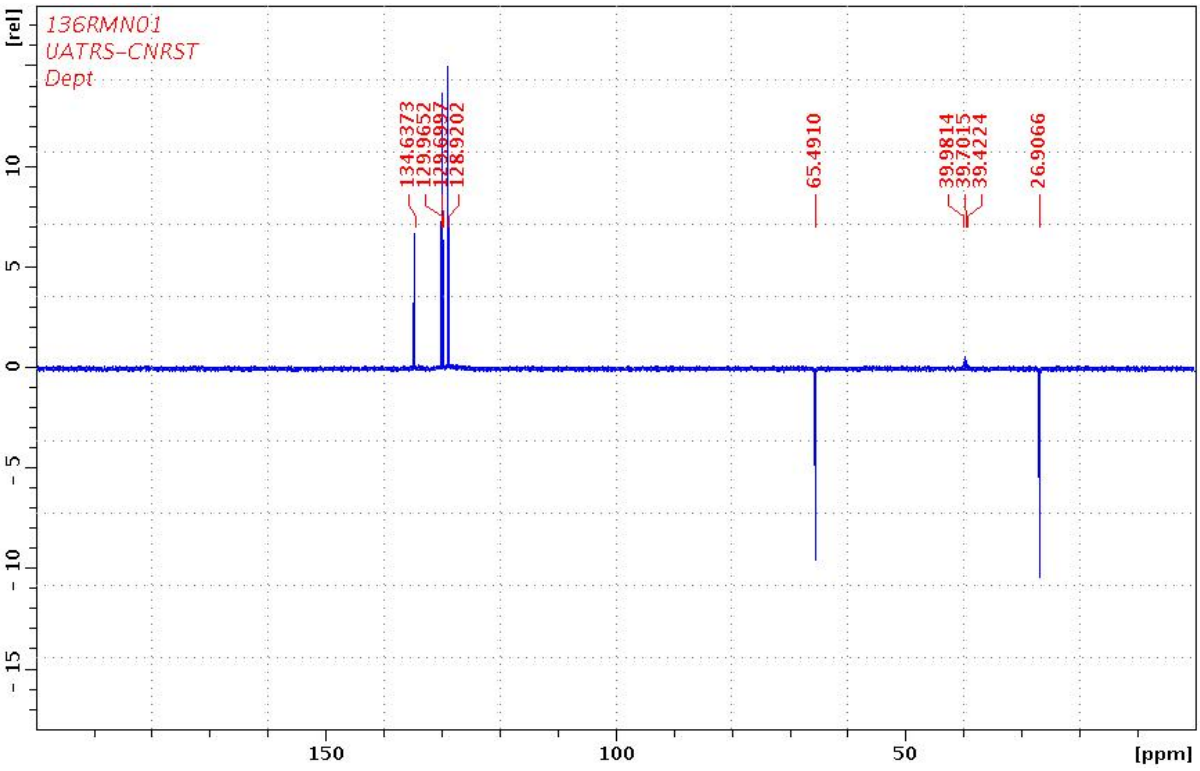

Figure S2: Dept-^{13}C-NMR spectrum of α-benzelidenyl- γ-butyrolactone (**3a**)

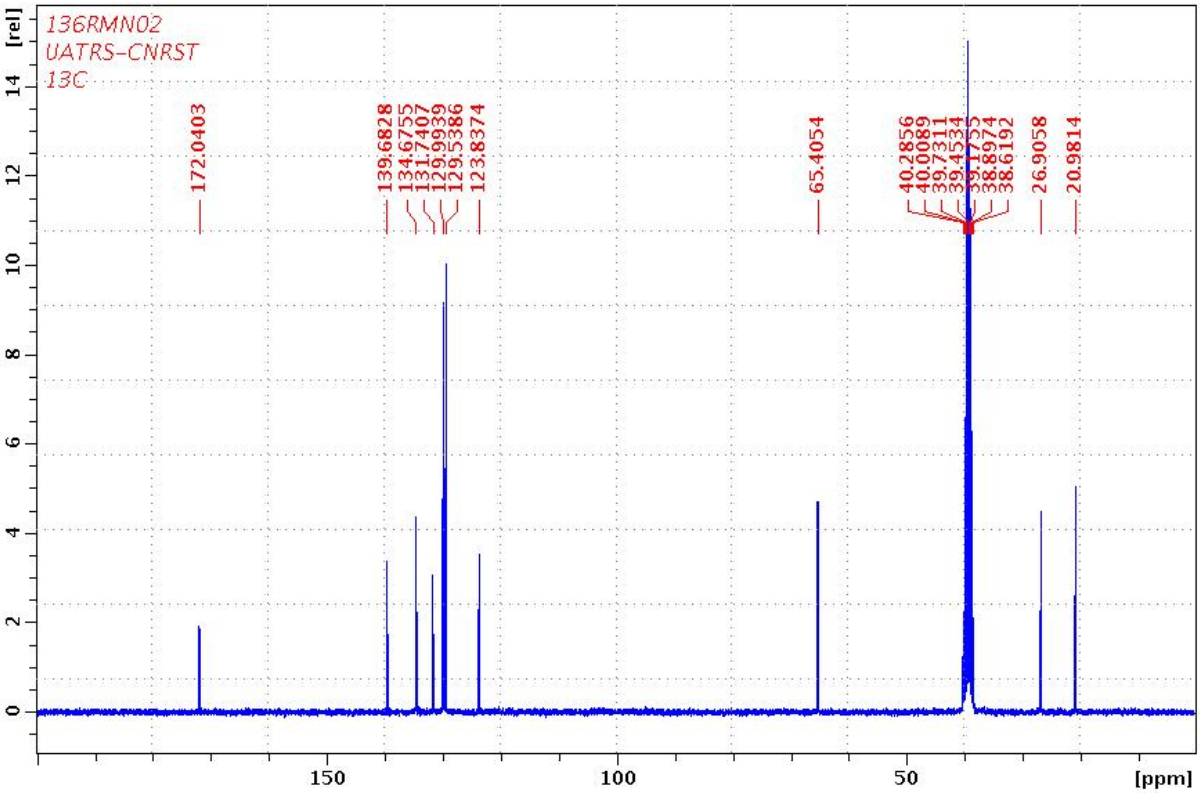

Figure S3: ^{13}C-NMR spectrum of α- (p-methylbenzelidényl)-γ-butyrolactone (**3b**)

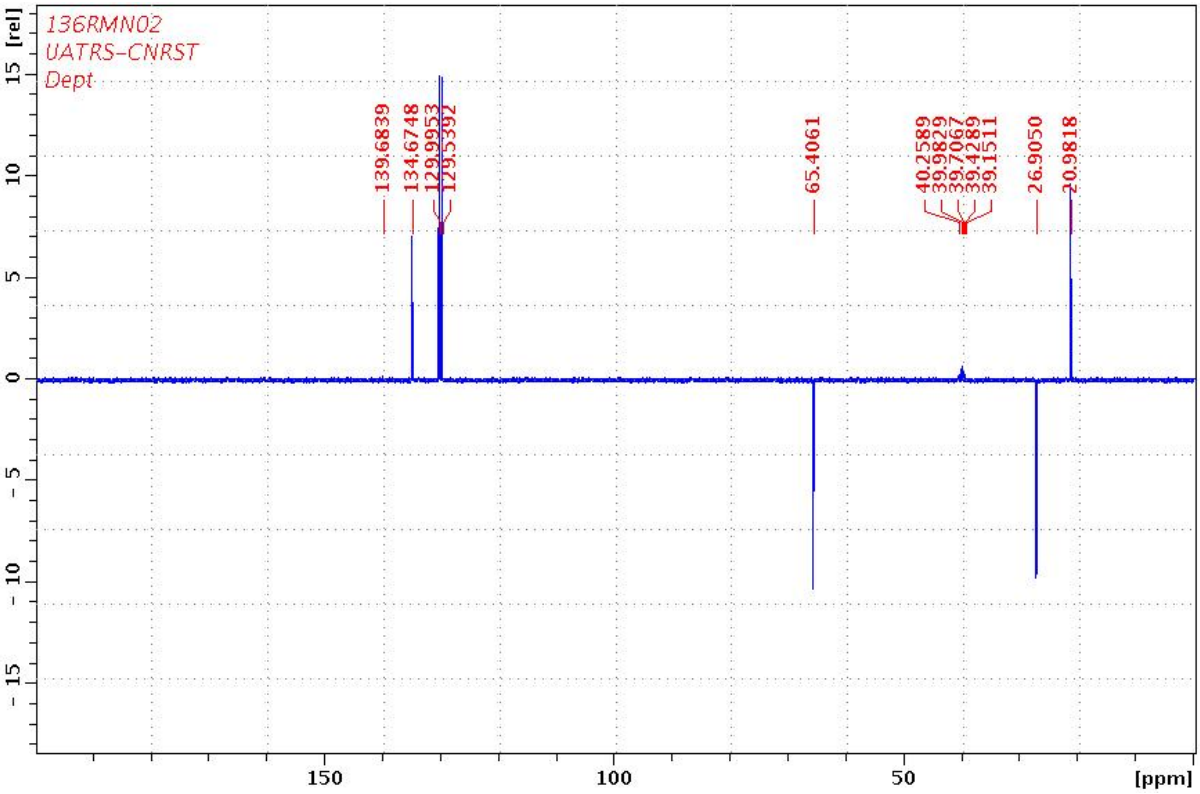

Figure S4: Dept-^{13}C-NMR spectrum of α- (p-methylbenzelidényl)-γ-butyrolactone (**3b**)

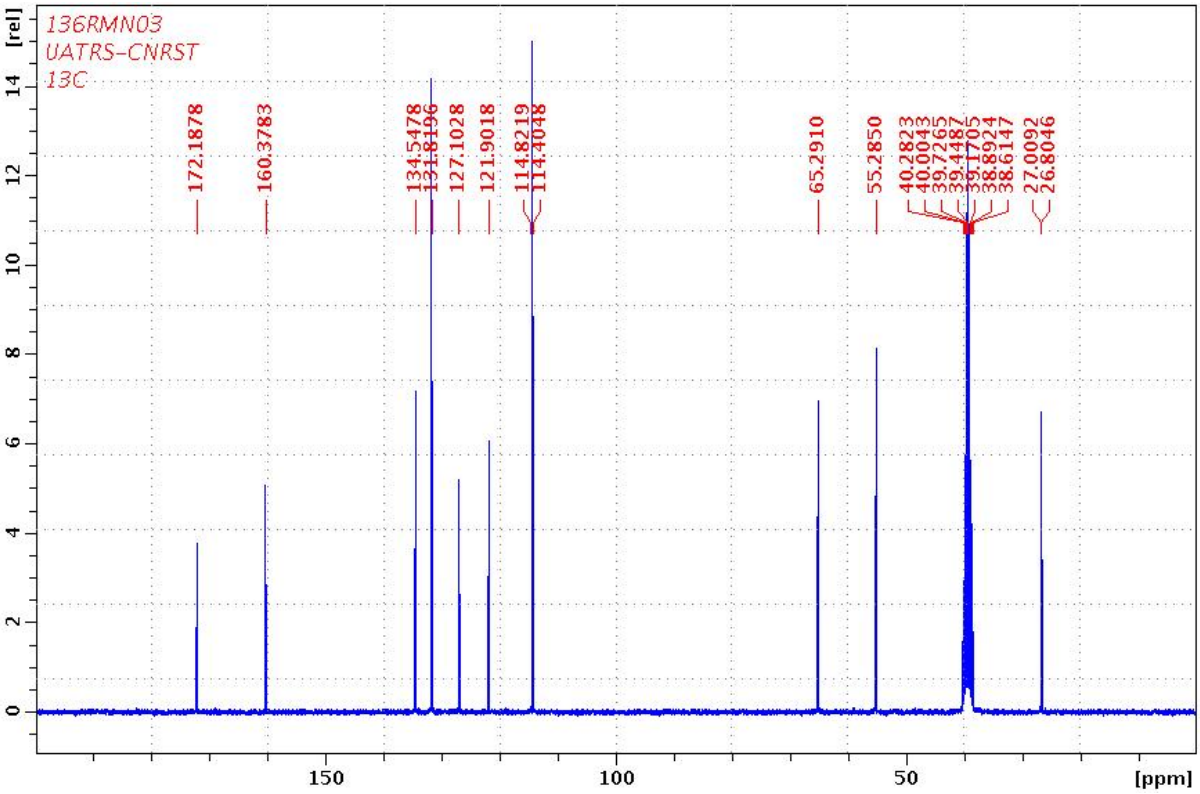

Figure S5: ^{13}C-NMR spectrum of α-(p-methoxybenzelidényl)-γ-butyrolactone (**3c**)

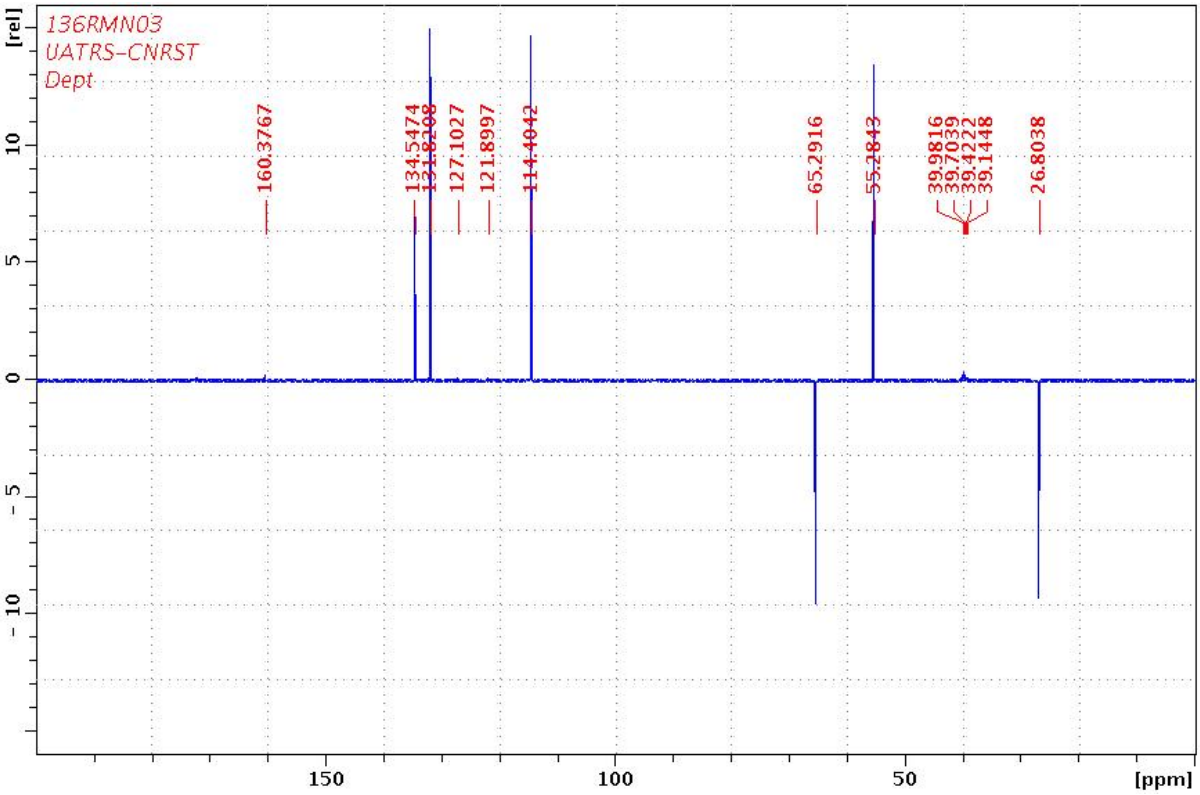

Figure S6: Dept-^{13}C-NMR spectrum of α-(p-methoxybenzelidényl)-γ-butyrolactone (**3c**)

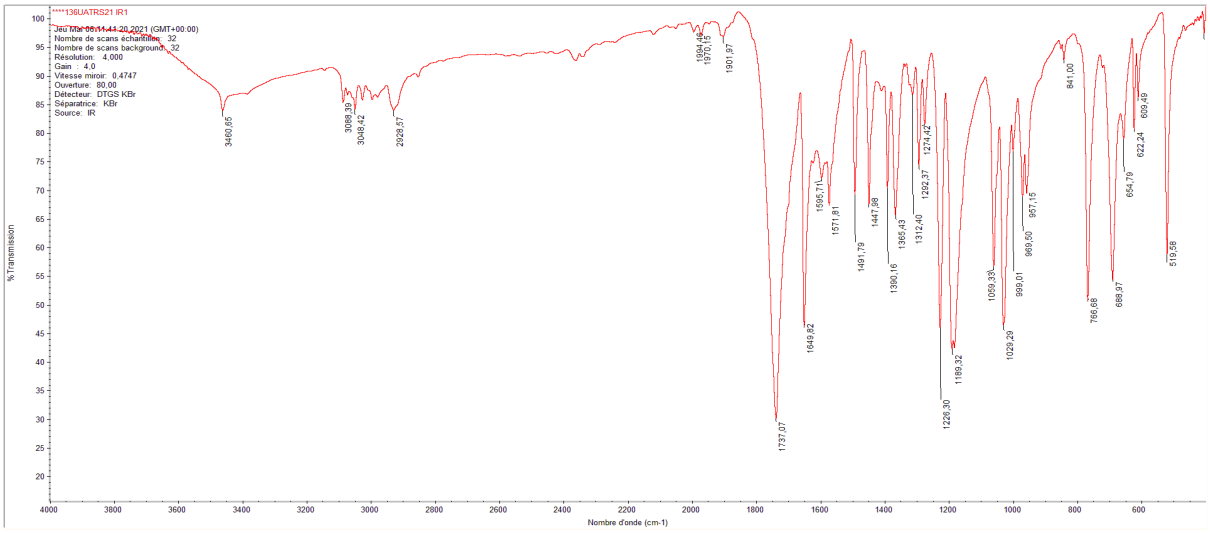

Figure S7: IR spectrum of α-benzelidenyl- γ-butyrolactone (**3a**)

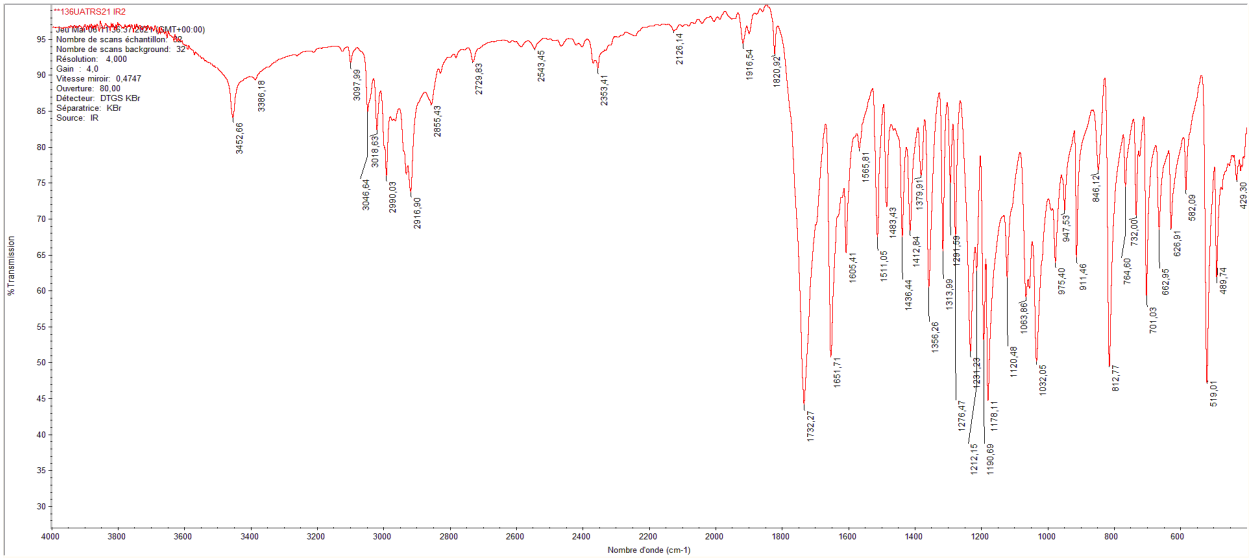

Figure S8: IR spectrum of α- (p-methylbenzelidényl)-γ-butyrolactone (**3b**)

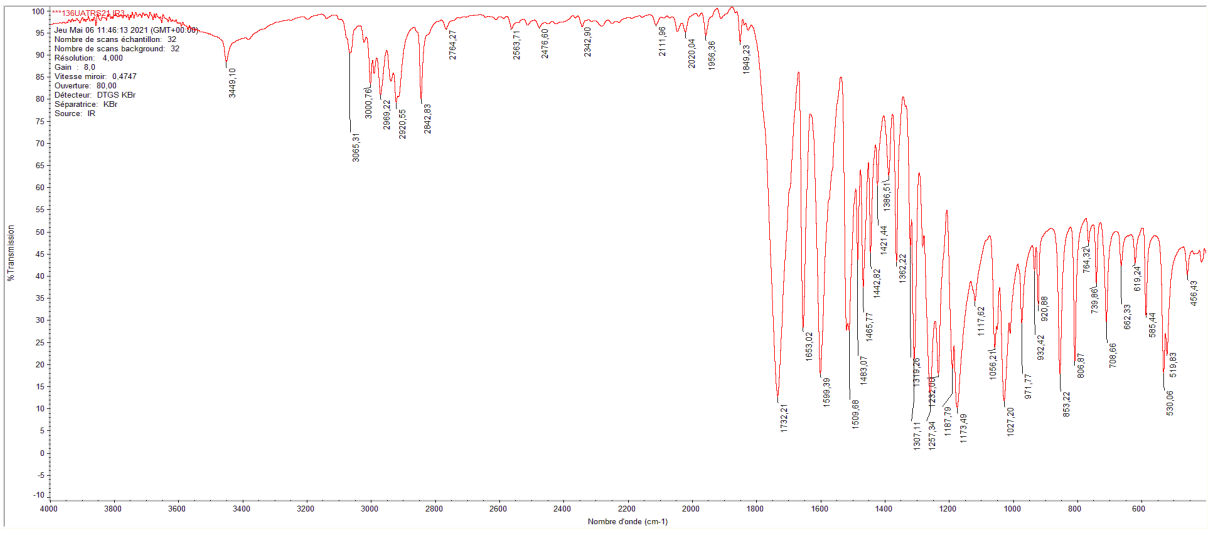

Figure S9: IR spectrum of α-(p-methoxybenzelidényl)-γ-butyrolactone (**3c**)

Crystal properties for α- (p-methylbenzelidényl)-γ-butyrolactone (3b)
Table S1: Crystal data

Chemical formula	$C_{12}H_{12}O_2$
M_r	188.22
Crystal system, space group	Monoclinic, $P2_1$
Temperature (K)	296
a, *b*, *c* (Å)	6.1893 (6), 5.2128 (4), 15.1000 (13)
□ (°)	90.994 (3)
V (Å^3)	487.11 (7)
Z	2
Radiation type	Mo *K*□
□ (mm^{-1})	0.09
Crystal size (mm)	0.35 × 0.26 × 0.19
Data collection	
Diffractometer	Bruker D8 VENTURE Super DUO
Absorption correction	Multi-scan *SADABS*(Krause et al., 2015)
T_{min}, T_{max}	0.667, 0.746
No. of measured, independent and observed [*I*> 2□(*I*)] reflections	26797, 2983, 2766
R_{int}	0.033
(sin □/□)$_{max}$ (Å^{-1})	0.714
Refinement	
R[*F*^{2}> 2□(*F*^{2})], *wR*(*F*^{2}), *S*	0.037, 0.109, 1.08
No. of reflections	2983
No. of parameters	128
No. of restraints	1
H-atom treatment	H-atom parameters constrained
□□$_{max}$, □□$_{min}$ (e Å^{-3})	0.20, -0.21
Absolute structure	Flack x determined using 1189 quotients [(I+)-(I-)]/[(I+)+(I-)] (Parsons, Flack and Wagner, ActaCryst. B69 (2013) 249-259).
Absolute structure parameter	0.4 (3)

Computer programs: *APEX3* (Bruker, 2016), *SAINT* (Bruker, 2016), *SAINT*, *SHELXTL2014*/7 (Sheldrick, 2015a), *SHELXL2014*/7 (Sheldrick, 2015b), *ORTEP-3* (Farrugia, 2012), *Mercury* (Macrae*et al.*, 2008);*publCIF* (Westrip, 2010).

Table S2: Hydrogen-bond geometry (Å, º) for (shelx)

D—H···*A*	*D*—H	H···*A*	*D*···*A*	*D*—H···*A*
C8—H4···O2^{i}	0.97	2.56	3.317 (2)	135
C8—H4···O2^{i}	0.97	2.56	3.317 (2)	135

Symmetry code: (i) *x*-1, *y*, *z*.
Data collection: *APEX3* (Bruker, 2016); cell refinement: *SAINT* (Bruker, 2016); data reduction: *SAINT*; program(s) used to solve structure: *SHELXTL2014*/7 (Sheldrick, 2015a); program(s) used to refine structure: *SHELXL2014*/7 (Sheldrick, 2015b); molecular graphics: *ORTEP-3* (Farrugia, 2012); software used to prepare material for publication: *Mercury* (Macrae*et al.*, 2008); *publCIF* (Westrip, 2010).
Document origin: *publCIF* [Westrip, S. P. (2010). *J. Apply. Cryst.*, **43**, 920-925].

Computing detail
Table S3: Crystal data

$C_{12}H_{12}O_2$	*F*(000) = 200
M_r = 188.22	D_x = 1.283 Mg m^{-3}
Monoclinic, $P2_1$	Mo *K*□ radiation, □ = 0.71073 Å
a = 6.1893 (6) Å	Cell parameters from 2983 reflections
b = 5.2128 (4) Å	□ = 2.7_30.5°
c = 15.1000 (13) Å	□ = 0.09 mm^{-1}
□ = 90.994 (3)°	*T* = 296 K
V = 487.11 (7) Å^3	Block, colorless
Z = 2	0.35 × 0.26 × 0.19 mm

Table S4: Data collection

Bruker D8 VENTURE Super DUO diffractometer	2983 independent reflections
Radiation source: INCOATEC I□S micro-focus source	2766 reflections with *I*> 2□(*I*)
HELIOS mirror optics monochromator	R_{int} = 0.033
Detector resolution: 10.4167 pixels mm^{-1}	□$_{max}$ = 30.5°, □$_{min}$ = 2.7°
□ and □ scans	*h* = -8□8
Absorption correction: multi-scan *SADABS*(Krause et al., 2015)	*k* = -7□7
T_{min} = 0.667, T_{max} = 0.746	*l* = -21□21
26797 measured reflections	

Table S5: Refinement

Refinement on F^2	Hydrogen site location: inferred from neighbouring sites
Least-squares matrix: full	H-atom parameters constrained
$R[F^2 > 2\sigma(F^2)] = 0.037$	$w = 1/[\sigma^2(F_o^2) + (0.0691P)^2 + 0.0285P]$ where $P = (F_o^2 + 2F_c^2)/3$
$wR(F^2) = 0.109$	$(\Delta/\sigma)_{max} < 0.001$
$S = 1.08$	$\Delta\rho_{max} = 0.20$ e Å^{-3}
2983 reflections	$\Delta\rho_{min} = -0.21$ e Å^{-3}
128 parameters	Absolute structure: Flack x determined using 1189 quotients [(I+)-(I-)]/[(I+)+(I-)] (Parsons, Flack and Wagner, ActaCryst. B69 (2013) 249-259).
1 restraint	Absolute structure parameter: 0.4 (3)

Special details

Geometry. All esds (except the esd in the dihedral angle between two l.s. planes) are estimated using the full covariance matrix. The cell esds are taken into account individually in the estimation of esds in distances, angles and torsion angles; correlations between esds in cell parameters are only used when they are defined by crystal symmetry. An approximate (isotropic) treatment of cell esds is used for estimating esds involving l.s. planes.

Table S6. Fractional atomic coordinates and isotropic or equivalent isotropic displacement parameters (Å^2) for (shelx)

	x	*y*	*z*	U_{iso}*/U_{eq}
O1	0.44262 (18)	-0.1397 (2)	0.55317 (8)	0.0424 (3)
O2	0.74041 (19)	-0.0707 (3)	0.63398 (10)	0.0536 (4)
C1	0.1001 (4)	1.1379 (4)	0.92825 (13)	0.0587 (5)
H11	0.1509	1.3017	0.9083	0.088*
H1	0.1391	1.1154	0.9896	0.088*
H10	-0.0542	1.1303	0.9213	0.088*
C2	0.2015 (3)	0.9281 (3)	0.87417 (11)	0.0438 (4)
C3	0.4066 (3)	0.8347 (4)	0.89444 (12)	0.0520 (4)
H7	0.4828	0.9009	0.9429	0.062*

C4	0.4990 (3)	0.6446 (4)	0.84359 (11)	0.0469 (4)
H6	0.6361	0.5845	0.8589	0.056*
C5	0.3910 (2)	0.5403 (3)	0.76957 (9)	0.0365 (3)
C6	0.4977 (2)	0.3371 (3)	0.72040 (10)	0.0376 (3)
H5	0.6374	0.2978	0.7396	0.045*
C7	0.4237 (2)	0.1992 (3)	0.65170 (9)	0.0332 (3)
C8	0.2154 (2)	0.2039 (3)	0.60027 (10)	0.0378 (3)
H12	0.2002	0.3623	0.5670	0.045*
H4	0.0932	0.1863	0.6392	0.045*
C9	0.2316 (3)	-0.0265 (3)	0.53815 (11)	0.0414 (3)
H3	0.1191	-0.1501	0.5507	0.050*
H2	0.2153	0.0281	0.4770	0.050*
C10	0.0938 (3)	0.8270 (4)	0.80088 (11)	0.0442 (4)
H8	-0.0433	0.8879	0.7860	0.053*
C11	0.1852 (3)	0.6379 (3)	0.74942 (10)	0.0412 (3)
H9	0.1088	0.5745	0.7006	0.049*
C12	0.5581 (2)	-0.0103 (3)	0.61514 (10)	0.0367 (3)

Atomic displacement parameters (Å^2) for (shelx)

	U^{11}	U^{22}	U^{33}	U^{12}	U^{13}	U^{23}
O1	0.0386 (5)	0.0421 (6)	0.0464 (6)	0.0018 (4)	-0.0033 (4)	-0.0068 (5)
O2	0.0325 (6)	0.0659 (9)	0.0623 (8)	0.0082 (6)	-0.0034 (5)	-0.0102 (6)
C1	0.0777 (13)	0.0475 (10)	0.0514 (9)	0.0030 (9)	0.0164 (9)	-0.0056 (8)
C2	0.0548 (9)	0.0395 (8)	0.0374 (7)	-0.0021 (7)	0.0096 (6)	0.0030 (6)
C3	0.0588 (10)	0.0561 (10)	0.0408 (7)	-0.0036 (9)	-0.0074 (7)	-0.0092 (8)
C4	0.0409 (8)	0.0553 (10)	0.0442 (7)	0.0005 (7)	-0.0085 (6)	-0.0071 (7)
C5	0.0358 (7)	0.0415 (7)	0.0321 (6)	-0.0038 (5)	-0.0004 (5)	0.0012 (5)
C6	0.0303 (6)	0.0453 (8)	0.0371 (6)	-0.0009 (6)	-0.0026 (5)	0.0009 (6)
C7	0.0264 (5)	0.0387 (7)	0.0345 (6)	-0.0019 (5)	0.0005 (4)	0.0031 (5)
C8	0.0300 (6)	0.0419 (7)	0.0413 (6)	0.0001 (5)	-0.0050 (5)	-0.0010 (6)
C9	0.0358 (7)	0.0425 (8)	0.0457 (7)	-0.0029 (6)	-0.0076 (5)	-0.0033 (6)
C10	0.0427 (8)	0.0476 (9)	0.0425 (7)	0.0039 (7)	0.0029 (6)	0.0034 (7)
C11	0.0388 (7)	0.0488 (9)	0.0358 (6)	0.0015 (6)	-0.0025 (5)	-0.0006 (6)
C12	0.0311 (6)	0.0414 (7)	0.0375 (6)	-0.0014 (5)	0.0015 (5)	0.0009 (6)

Geometric parameters (Å, º) for (shelx)

O1—C12	1.3481 (19)	C5—C6	1.458 (2)
O1—C9	1.448 (2)	C6—C7	1.337 (2)
O2—C12	1.2012 (19)	C6—H5	0.9300
C1—C2	1.508 (3)	C7—C12	1.485 (2)
C1—H11	0.9600	C7—C8	1.4938 (18)
C1—H1	0.9600	C8—C9	1.528 (2)
C1—H10	0.9600	C8—H12	0.9700
C2—C10	1.386 (2)	C8—H4	0.9700
C2—C3	1.389 (3)	C9—H3	0.9700
C3—C4	1.384 (3)	C9—H2	0.9700
C3—H7	0.9300	C10—C11	1.382 (2)
C4—C5	1.402 (2)	C10—H8	0.9300
C4—H6	0.9300	C11—H9	0.9300
C5—C11	1.400 (2)		

C12—O1—C9	111.76 (12)	C6—C7—C8	132.54 (14)
C2—C1—H11	109.5	C12—C7—C8	107.61 (12)
C2—C1—H1	109.5	C7—C8—C9	103.95 (12)
H11—C1—H1	109.5	C7—C8—H12	111.0
C2—C1—H10	109.5	C9—C8—H12	111.0
H11—C1—H10	109.5	C7—C8—H4	111.0
H1—C1—H10	109.5	C9—C8—H4	111.0
C10—C2—C3	117.88 (16)	H12—C8—H4	109.0
C10—C2—C1	120.61 (17)	O1—C9—C8	107.03 (12)
C3—C2—C1	121.49 (17)	O1—C9—H3	110.3
C4—C3—C2	120.95 (16)	C8—C9—H3	110.3
C4—C3—H7	119.5	O1—C9—H2	110.3
C2—C3—H7	119.5	C8—C9—H2	110.3
C3—C4—C5	121.61 (15)	H3—C9—H2	108.6
C3—C4—H6	119.2	C11—C10—C2	121.59 (16)
C5—C4—H6	119.2	C11—C10—H8	119.2
C11—C5—C4	116.83 (15)	C2—C10—H8	119.2
C11—C5—C6	124.88 (13)	C10—C11—C5	121.13 (15)
C4—C5—C6	118.28 (14)	C10—C11—H9	119.4

C7—C6—C5	129.31 (14)	C5—C11—H9	119.4
C7—C6—H5	115.3	O2—C12—O1	121.18 (16)
C5—C6—H5	115.3	O2—C12—C7	129.40 (15)
C6—C7—C12	119.82 (13)	O1—C12—C7	109.41 (12)

C10—C2—C3—C4	-0.7 (3)	C7—C8—C9—O1	-2.57 (16)
C1—C2—C3—C4	-179.11 (19)	C3—C2—C10—C11	0.4 (3)
C2—C3—C4—C5	0.5 (3)	C1—C2—C10—C11	178.81 (17)
C3—C4—C5—C11	0.1 (3)	C2—C10—C11—C5	0.2 (3)
C3—C4—C5—C6	-178.86 (17)	C4—C5—C11—C10	-0.4 (2)
C11—C5—C6—C7	-3.1 (3)	C6—C5—C11—C10	178.46 (16)
C4—C5—C6—C7	175.75 (16)	C9—O1—C12—O2	-177.19 (16)
C5—C6—C7—C12	-176.46 (15)	C9—O1—C12—C7	3.33 (17)
C5—C6—C7—C8	1.4 (3)	C6—C7—C12—O2	-6.0 (3)
C6—C7—C8—C9	-173.67 (16)	C8—C7—C12—O2	175.61 (18)
C12—C7—C8—C9	4.42 (15)	C6—C7—C12—O1	173.42 (14)
C12—O1—C9—C8	-0.42 (18)	C8—C7—C12—O1	-4.96 (16)

Hydrogen-bond geometry (Å, º) for (shelx)

D—H···*A*	*D*—H	H···*A*	*D*···*A*	*D*—H···*A*
C8—H4···O2^{i}	0.97	2.56	3.317 (2)	135
C8—H4···O2^{i}	0.97	2.56	3.317 (2)	135

Symmetry code: (i) *x*-1, *y*, *z*.
Document origin: *publCIF* [Westrip, S. P. (2010). *J. Apply. Cryst.*, **43**, 920-925].

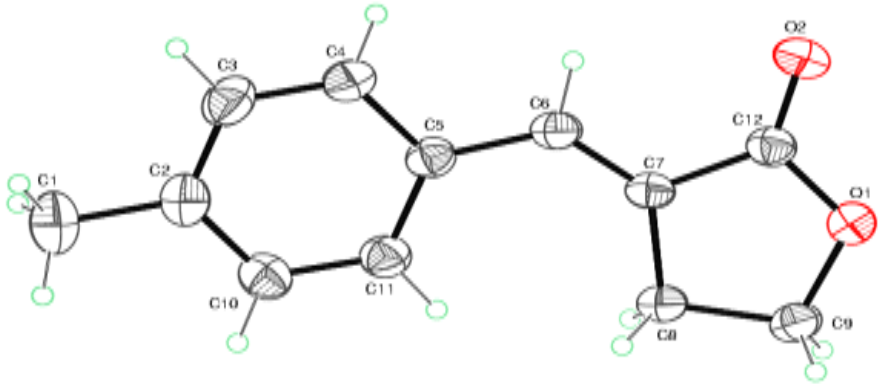

(2023) ; https://revues.imist.ma/index.php/morjchem/index